Omar El Ouahabi El Ouahabi

DETECTION OF THE ANGLE OF ROTATION OF A RETRO-REFLECTIVE WRISTBAND BY MEANS OF VISIBLE LIGHT SENSING

MASTER THESIS

Directed by, Dr. Hugo Valderrama Blaví

MEVTECH

UNIVERSITAT ROVIRA I VIRGILI

Tarragona

2022

Thanks to the Rovira i Virgili University for all these years of training, especially to the ETSE and Dr. Hugo Valderrama Blaví for being so dedicated and patient towards me.

Thanks also to the company Joanneum Research for this magnificent experience in the SCL Materials group where I hope to grow my professional skills in the world of electronics.

INDEX

Abstract

Since the rise of the implementation of LED (light-emitting diodes) in the daily life, other technologies apart from basic lighting are taking place in the world of the Internet of Things (IoT), the ability to use the artificial lighting for purposes such as communication, indoor positioning, identification of objects based on their reflectivity, etc. They are showing enormous potential in the present Industrial Revolution 4.0. In this article, we present a simple, cost-effective, novel approach to identify the angle of rotation of a rotational device through Visible light sensing in addition to the identification of the lighting conditions in which it is found.

1. Introduction

Since the arrival of the 4th industrial revolution [1] [2] and the standardization of LED based luminaires [3], they have gone from not only providing basic lighting for day to day, but also have proven to be capable of providing characteristics such as establishing communication via light, known as Visible light communication (VLC) [4] [5], or positioning tasks via light, known as Visible light positioning (VLP) [6] [7]. In addition to the VLC and VLP functionalities there is another functionality based on analysing reflected light (on surfaces of different colours and shapes) called Visible light sensing (VLS) [8] [9] [10]. This article will show the promising functionalities of this technology that is being the focus of increased research in recent years.

Taking advantage of the versatility of LED devices to be able to modulate their intensity and the spectral power distribution with frequencies that are imperceptible to human beings [11] but are perceptible by a receiver, such as a photodiode [12], we can use a width of frequencies outside of those commonly used by , for example, Wi-Fi, Radio, TV, Bluetooth, etc.

Likewise, with its high bandwidth and low latency, VLC technology is a candidate to consider relieving the congested RF network that we have nowadays.

Another of the many advantages of the VLC and VLS is its security [13] against external threats, since being a system that could be mounted indoors, reusing the previous infrastructure, the same physical walls that surround it act as a firewall against external attacks.

Also, with the VLS advantages, the conventional passive control devices like sensors cameras, etc., which have an added complexity of design, implementation, cost and also an added energy consumption could be avoided and replaced by any of the visual light technologies mentioned previously which can be implemented reusing the same lighting infrastructure.

Due to the characteristics already mentioned and the low-cost, VLS could have a very important role in industrial applications, or in the day-to-day life of people integrating into the Internet of Things (IoT) [14].

1.1 State of the art

To date, many investigations have taken place in this area, such as, the identification of manual gestures by means of photodiodes and machine learning algorithms as discussed in [15], or for example in [16], it is shown thate from the reflections of foils placed on the roof of vehicles can be used to sense its parameters. At the same time, it has also been demonstrated how through VLS it has been possible to detect human presence [17], and/or their location (LiDaL) [18]. Among many other applications, LEDs also have the advantage of being able to switch between different light intensities at a very fast rate. This capability has spawned a new communication method (as already described, VLC) in which LED luminaires can be employed for high-speed data transmission.

1.2 VLS, VLP and VLC in the automotive context

Among these applications, many VLC research groups are particularly interested in adapting VLC for Intelligent Transportation Systems (ITS). ITSs have taken advantage of the Information and Communication Technologies (ICT) to gain intelligence in transportation, giving a variety of technological methods to assist users. ITSs are presently investigating the usage of VLC as one of the possible ICTs, concentrating on two factors. First and foremost, transportation lighting infrastructure can be used for communication. LEDs are being used in transportation lighting infrastructure such as streetlamps, traffic signals, and automobile lamps. As a result, in the case of an ITS based-on VLC, traditional automobile and traffic LEDs will be able to be used. As a result, the cost of developing the ITS infrastructure will be lower. Second, because visible light and traditional RF communications occupy distinct regions of the electromagnetic spectrum, the electromagnetic compatibility problem, which is a severe issue with ITSs based on RF signals, will be minimized. In figure 1 some scenarios outlining how VLS, VLP and/or VLC can be used in this context, are given.

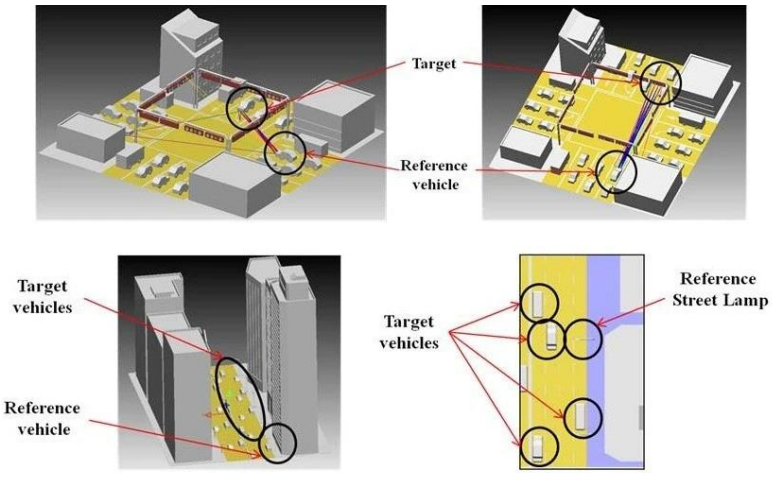

Figure 1 VLC ITS usage in different scenarios, urban & metropolitan [19].

1.3 Objectives

The main goal of this project is to show a novel application of VLS technology in the world of Industry 4.0, demonstrating the ability to determine the angle of rotation of a robotic arm through reflected light of the reflective foils that are attached to the robotic arm, which have different colours, and shapes. All in different scenarios.

In industrial applications where robotic arms are routinely utilized, such a system would have enormous potential. In this paper, we illustrate how our suggested method can solve some of the issues that are emerging for IoT applications by building a system that does not require active motion detection and control sensors on the robotic arm. Furthermore, we will demonstrate that by combining the VLS task of sensing the rotation of the robotic arm with the functionality of data transmission via VLC, an RF-free infrastructure is created, allowing us to avoid the previously mentioned problems with interferences and spectrum limitations predicted for future RF communication.

We will also demonstrate that with machine learning assisted VLS, a system can be developed that takes minimal training effort for ML model creation and allows for high accuracies in robotic arm rotation determination. We show that our solution approach is also resilient to environmental changes using the experimental data reported in this project.

1.4 K-Nearest Neighbour machine learning algorithm

To make reliable predictions, K-Nearest Neighbour (KNN) uses observable data similarities and advanced distance measurements. This strategy may appear contradictory and untrustworthy at first, yet it is quite trustworthy.

KNN is a non-parametric method that is used for lazy learning. It predicts the categorization of a new sample point based on data from numerous classes. Because it makes no assumptions

about the data being investigated, KNN is a non-parametric method. The KNN technique saves all existing data and classifies new data points using the similarity measure (e.g., distance functions). When new data becomes available, this is what it implies. Then, using the KNN method, it may be quickly sorted into a suitable category.

The following are some of the benefits of KNN:

- Quick calculation.
- To interpret, a simple algorithm is used.
- Regression and classification are both possible with this model.
- High precision.
- There are no additional assumptions regarding data, and there is no need to modify numerous parameters or develop a model. This makes it vital in the case of nonlinear data.

KNN Has a Few Drawbacks

- The accuracy of the data is determined by its quality.
- With a lot of data, the prediction stage could take a long time.
- Sensitive to the size of the data and aspects that are not relevant
- High memory is required since all the training data must be stored.
- It can be computationally expensive because it stores all the training.

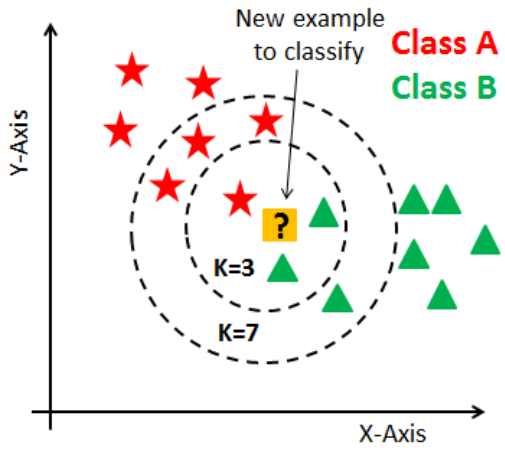

Figure 2 KNN Diagram example [20].

Based on the example given in figure 2 we can describe one of the issues that must be taken into account when using KNN. If we have one new example to classify in between two classes (Class A & Class B) as shown in figure 2, if we pre-set a number of neighbours of 1, since the 1st closest neighbour is the red star, it will be classified as a Class A. Nevertheless, if we pre-set a number of neighbours of 3, then the first neighbour is the red star and the second and third closes neighbours are green triangles, then the new example will be classified as a Class B.

Anyway, the way to calculate the distance in between the new example to classify and the clouds of training data can be calculated in different ways, for example, Euclidean Distance; Manhattan Distance; Minkowski Distance; Hamming Distance…

1.5 Solution approach

1.5.1 VLS unit 2.0

The hardware used in this work was introduced in [21]. Two main components make up the VLS Unit 2.0: an Ultra96-V2 board by AVNET Inc. and a self-developed PCB establishing a digital front-end as well as the A/D converter. In the Ultra96-V2 board, the processing unit is a Zynq UltraScaleCTM MPSoC that is based on the Arm architecture. The development board

has a small form factor (85mm x 54mm) and comes with a variety of built-in communication interfaces (WiFi, USB, Ethernet, etc.). MPSoC platforms have the advantage that while all time-critical aspects of the system, like control of the Analog-to-Digital converter (ADC), can be implemented in the FPGA part of the processing unit, less time-critical functions can be implemented in the System-on-a-chip (SoC) part. As part of the SoC, the advantage of having the option to use higher-level programming languages (e.g. C, C++) as well as higher-level peripheral access can be exploited. The fact that certain tasks can be assigned to each part of the processing unit is a huge benefit of the system, while reducing the software implementation effort. A custom-developed analog front end (PCB board), which attaches directly to the Ultra96-V2 board as a piggyback extension, contains two main subsystems along with other components, including power rail regulators, a level translator for the LED driver, and an I2C temperature sensor.

As can been seen in figure 4 CREE RGBW MCE LED [29] and a GaN-based LED driver circuit make up the transmitter module. There are four separate LED dies (for red, green, blue and white), which can be individually controlled. The EPC2040 GaN power transistor was used to modulate the individual LED dies. Despite its small size, this transistor can handle a large current at high switching rates. As a result of its ability to source and sink large amounts of current, the LMG1020 GaN low-side gate driver was chosen to control this FET, since it can rapidly rise and fall at high LED current modulation rates. The gate driver works with a 5 V logic level. A voltage level translator was used since the Ultra96-V2 board can only provide 3.3 V. Each die of the driver is designed to carry 350 mA individually. The LED current of each die was limited to 350 mA by a current limiting resistor. To carry 350 mA of current without any thermal issues, all resistors were chosen according to their wattage class ratings. Added heatsinks provide proper thermal design for these resistors. There are dedicated GPIOs on the Ultra96-V2 board for the input stage of the logic level translator. With its integrated

FPGA, the GPIOs can be easily controlled utilizing the ARMCortex on the Xilinx MPSoC (figure 6).

The PCB footprint for the LED has been designed in such a way as to allow proper heat dissipation by using a standard heat sink. In order to monitor the thermal performance of the PCB design, a temperature sensor was placed close to the LED. A software implemented PID unit controls a controllable fan at the heatsink to alter the thermal performance.

An 3-Channel/1Chip (R, G, B) Si photodiode colour sensor is used in the receiver module, which is based on a Kingbright APS5130PD7C P22 RGB colour sensor [22]. There is one amplifier and data-sampling channel for each photodiode in this colour sensor. Using transimpedance amplifiers (TIA) (figure 5) the photocurrent generated by photodiodes is amplified. As transimpedance amplifiers from Linear Technology Cooperation LTC6268-10 op-amps were used, since they do not have a large parasitic capacitance, have a low bias current, and have a wide bandwidth of up to 4GHz. A second identical colour sensor was used for dark current compensation, connected to the operational amplifiers' non-inverting inputs. A black tape covers the second colour sensor, so that no light impinges on the active area and only dark current is generated. As a result, the offset voltage caused by the dark current of the regular circuit will be cancelled at the output of the transimpedance amplifier. The second colour sensor is located on the bottom side of the PCB right below the main colour sensor.

An in-house 3D printer was used to create a housing for the VLS unit 2.0.. It has holes for fixing so that the entire device can be mounted on an aluminium structure for the experiments. Figure 3 shows the 3D model of the complete VLS unit 2.0 with the 3D printed housing.

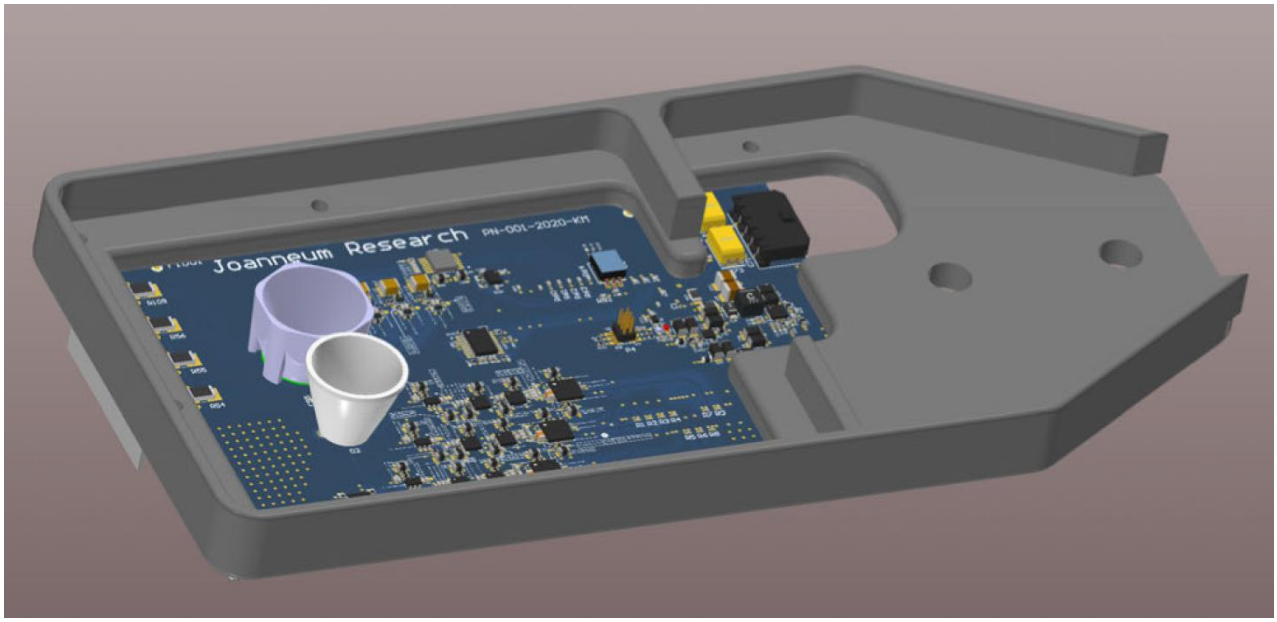

Figure 3 3D model of the VLS unit 2.0 & 3D printed housing [21].

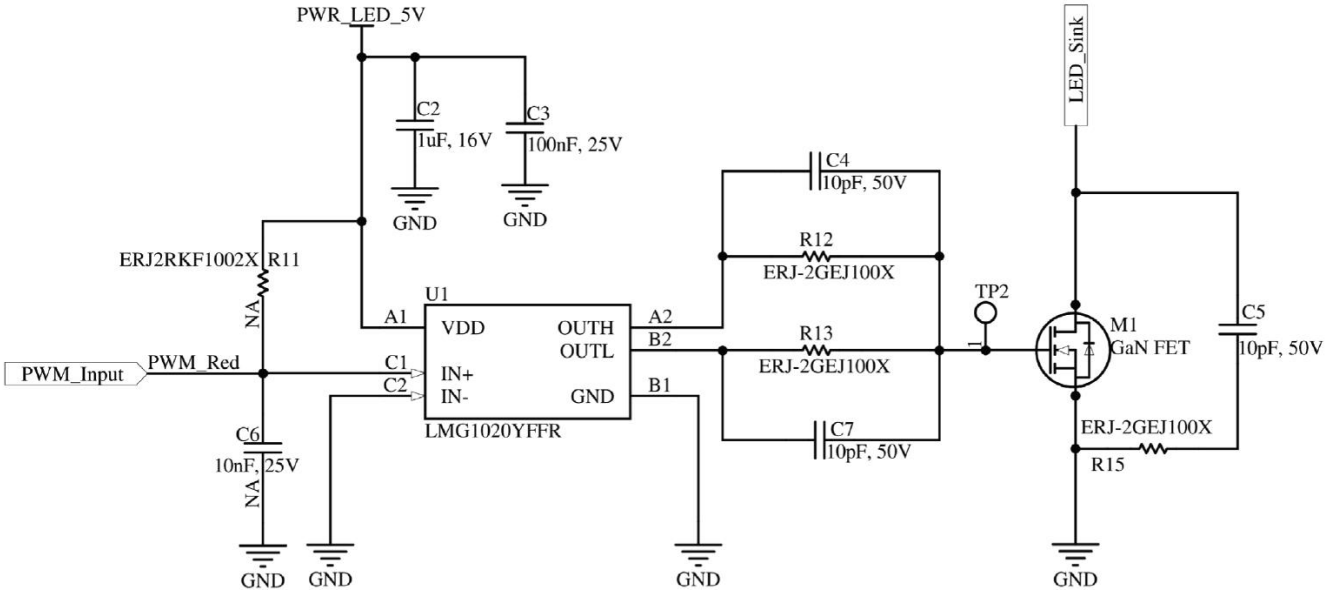

Figure 4 Single channel GaN FET-based LED driver circuit [21].

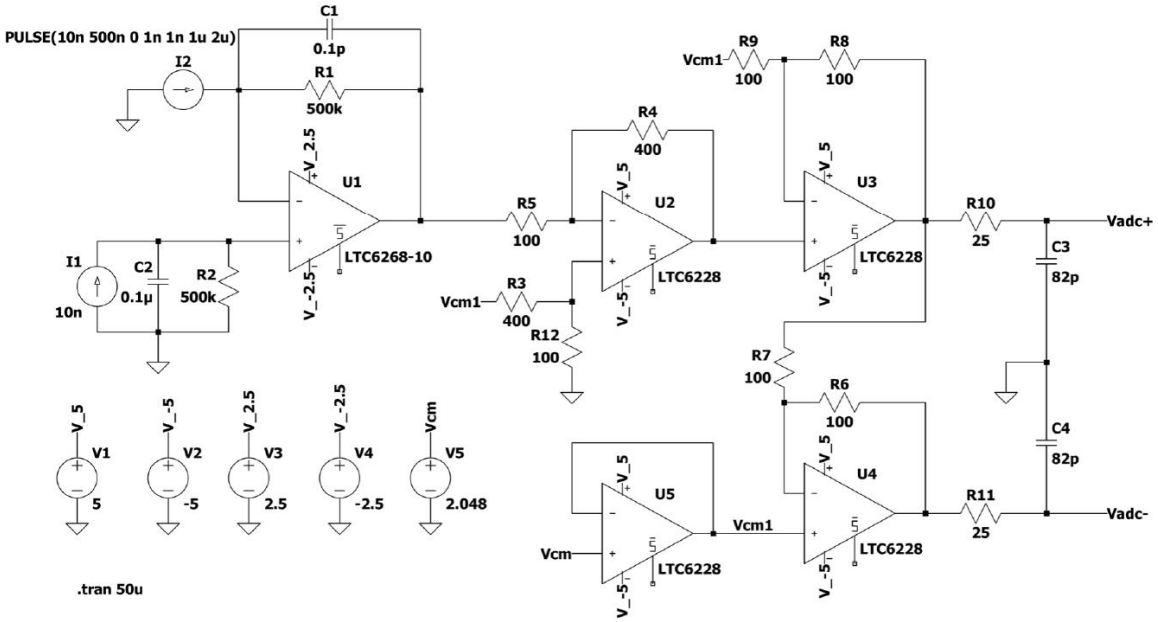

Figure 5 ADC driver circuit including transimpedance amplifier [21].

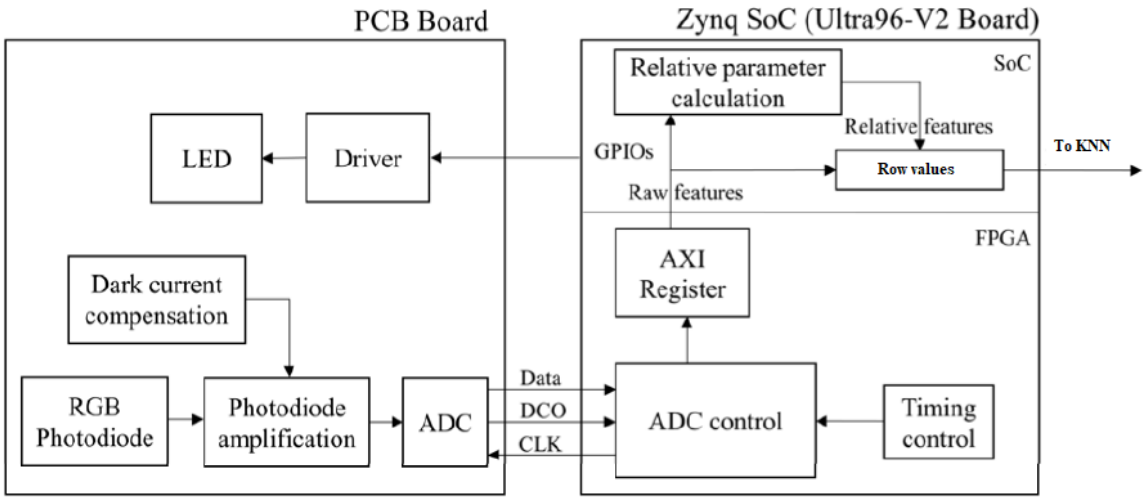

Figure 6 Block diagram of the FPGA and SoC implementations and the Interfaces between the PCB board and the Ultra96-V2 board [21].

1.5.2 Setup

The whole setup has been mounted in a corner in one of our laboratories with no furniture around it, with the walls painted white and a black mat on the floor to avoid possible unwanted reflections.

The setup consists of a robotic arm (Niryo One), from vendor Niryo [23], with the configuration of retroreflective foils around the arm. At 1.2 meters of distance respect the robot arm, the VLS unit 2.0 [21] has been placed by means of an aluminium structure. The following figure 7 shows the setup used in all the experiments.

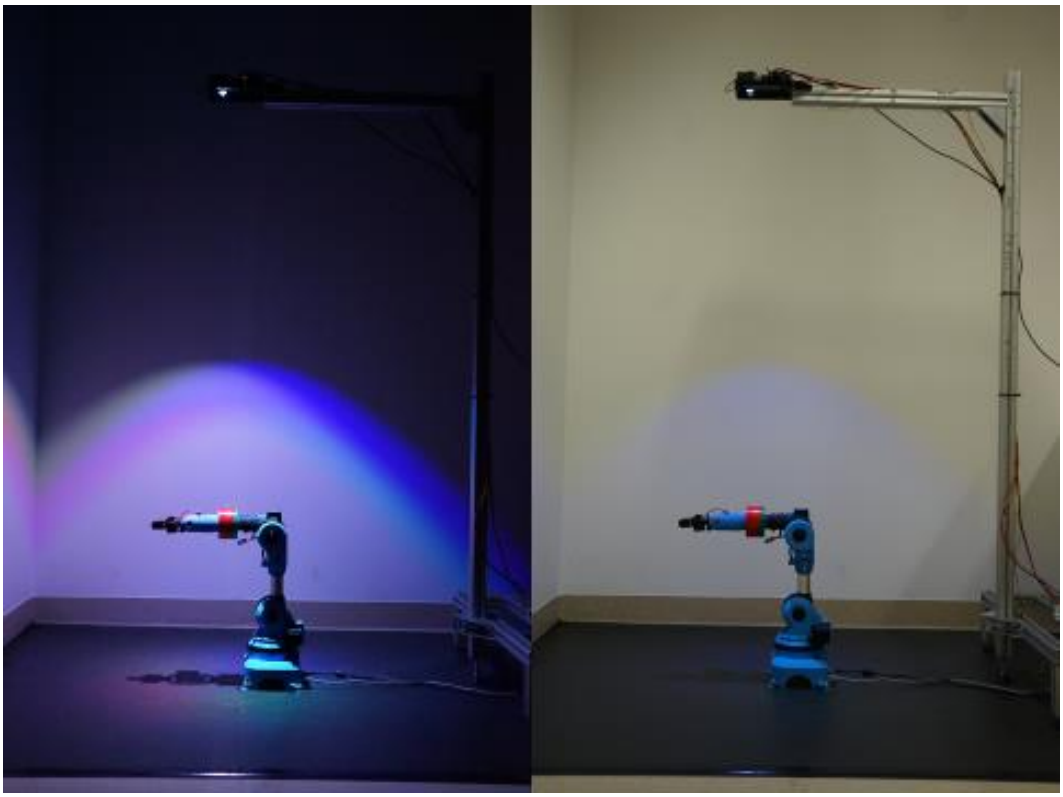

Figure 7 Experimental Setup.

Two different configurations of retroreflective foils, from the vendor 3M [24] , have been used, each of them attached to one piece of cylindrical cardboard, forming a kind of wristband, and with a 3D printed cylindrical plastic piece they were attached to the robotic arm. The two configurations are identified by the colours of which they are made. The first configuration being the red and green, used in the first scenario, and the red, green and blue configuration, used in the rest of the scenarios.

The figure 8 shows both configurations attached to the cylindrical cardboards, in the left side we see the red and green configuration and in the right side the red, green and blue configuration.

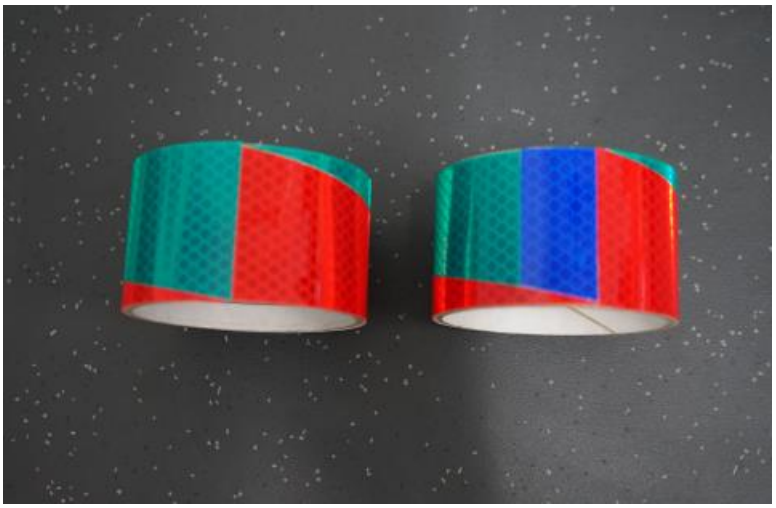

Figure 8 Retroreflective foils attached to the cylindrical cardboards.

The following figure 9 better shows in a 2D representation the two configurations used.

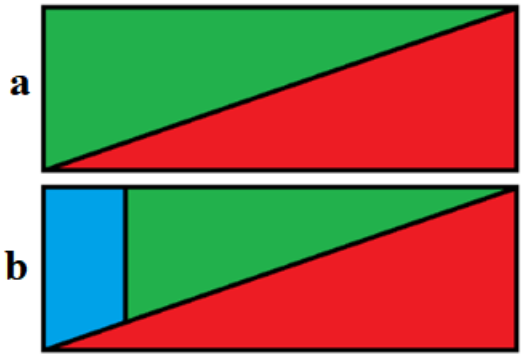

Figure 9 Foil distributions. (a) red and green. (b) red, green and blue.

To be able to reuse the same foils in case of changing the experiments scenario, a 3D printed cylindrical piece was used between the robotic arm and the wristband to attach both as it is shown in figure 10.

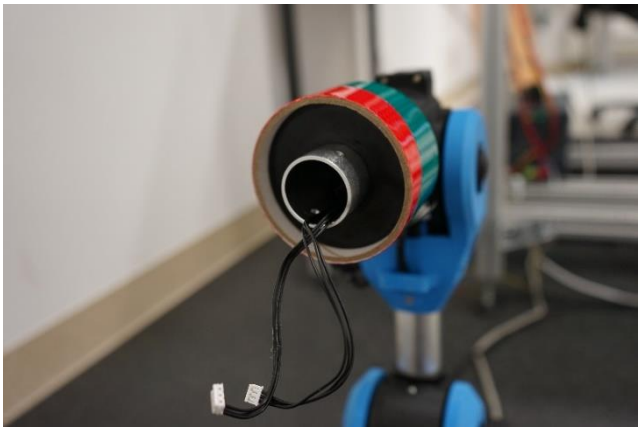

Figure 10 3D printed junction cylindrical piece.

The first lighting scenario in which the measurements have been carried out is with only the VLS unit 2.0 LED as a light source, having the fluorescent tubes of the laboratory turned off and with different wristbands and arm deviations. The second lighting scenario is having the LED from the VLS unit 2.0 and the luminaries (fluorescent tubes) of the room turned on to investigate the effect of having an additional source of light. In order to avoid external light sources, the whole set-up has been mounted in one of our laboratory rooms where the shades could be closed completely to block the sunlight. All the measurements referred to light have been measured with the UPRtek MK350S PREMIUM hand spectrometer [25].

To have enough data for the learning and testing phases, it has been decided to have 20 runs for each scenario, and thus be able to use 10 of them for the training phase and 10 of them for the testing phase. Each run is made up of 350 ° of rotation in 1º steps ranging from -175º to 175º. For each degree, a file has been obtained with 500 absolute values for each channel of the photodiode, that is, 500 red values, 500 green values and 500 blue values, from the respective channels of the RGB photodiode.

The average value of these 500 values will be the value that has been attributed to the angle of rotation of the run. From here, the relative values (which we will discuss subsequently in this chaptr) have been obtained.

Anticipating possible differences that may occur during the data collection process (changes in temperature during the day, different amounts of reflected light ...) it has been decided to avoid using the raw data that comes directly from the 3-channel RGB photodiode (red values, green values and blue values), which we will further refer to as absolute values. That is why, instead of directly using the absolute values, we employed relative parameters [21] calculated from the obtained absolute values as it is shown in table 1.

Table 1 **Relative parameters**

Relative parameter		Calculation from absolute values
Red_Green	=	Red - Green
Red_Blue	=	Red - Blue
Green_Blue	=	Green - Blue
Div_Red_Green	=	Red ÷ Green
Div_Red_Blue	=	Red ÷ Blue
Div_Green_Blue	=	Green ÷ Blue

In order to obtain results based in predictions, we used the Machine Learning K-Nearest Neighbour algorithm (KNN algorithm), which relies on 'feature similarity' to predict values of the new incoming data points from the data previously obtained, that from now on we will distinguish as "training data" to those values used to generate the model of the underlying scenario, and "test data" to those values used to be predicted in each scenario.

In figure 11 we can observe the overview of the proposed solution approach.

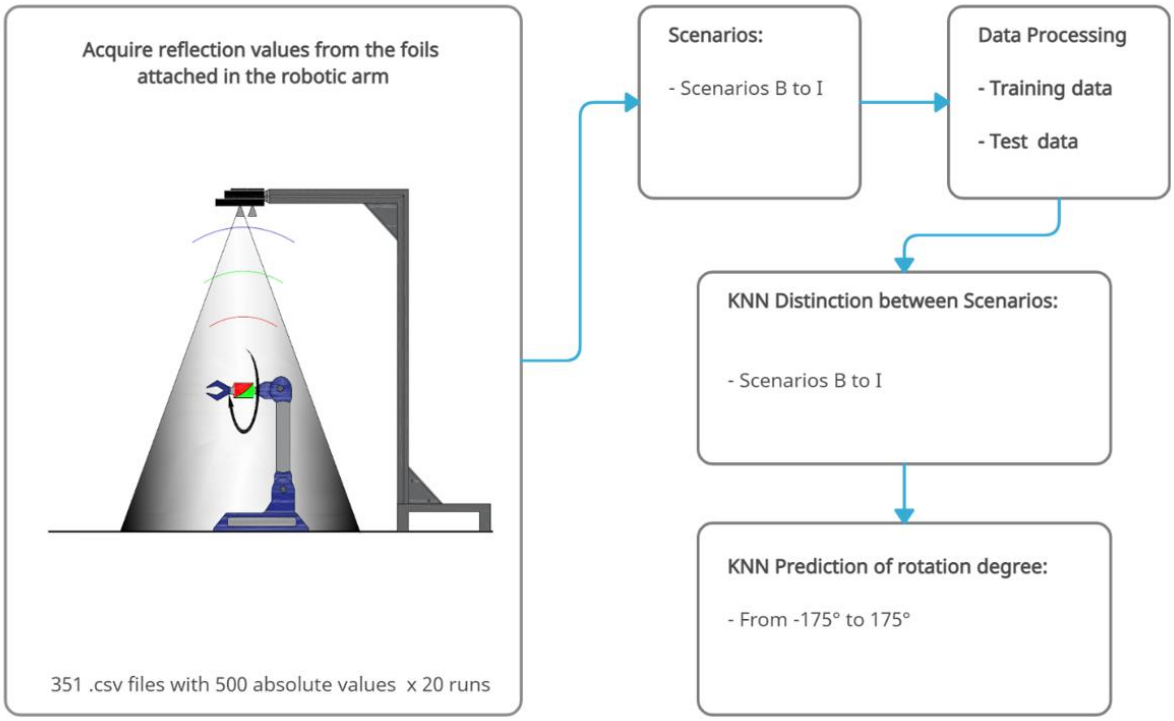

Figure 11 Overview of the solution approach

In summary, the order of experiments in different scenarios, in which the experiments were performed and the results will be shown and discussed, are given in table 2:

Table 2 **Experimental Scenarios**

Scenario	Type of wristband	Source of light	Distance	Arm deviation
A	Red and green	VLS unit 2.0 LED	1,2 m	0 º
B	Red, green and blue	VLS unit 2.0 LED	1,2 m	0 º
C	Red, green and blue	VLS unit 2.0 LED	1,2 m	Tilt +5º
D	Red, green and blue	VLS unit 2.0 LED	1,2 m	Tilt +10º
E	Red, green and blue	VLS unit 2.0 LED	1,2 m	Tilt -5º
F	Red, green and blue	VLS unit 2.0 LED	1,2 m	Tilt -10º
G	Red, green and blue	VLS unit 2.0 LED	1,2 m	Azimuth +5º
H	Red, green and blue	VLS unit 2.0 LED	1,2 m	Azimuth -5º
I	Red, green and blue	VLS unit 2.0 LED + Ambient light	1,2 m	0 º
B - I	Use of scenario B as test database and scenario I as test data for comparison			
Overall	Distinction of the scenarios B to I trough machine learning			

2. Results

Following the order described in the introduction, the characteristics for each scenario will be shown below as well as the results obtained in each of them. Furthermore measurements taken by the spectrometer, representations of the reflected light values obtained, prediction results for each angle of rotation and finally the percentage of success in the differentiation of scenarios will be shown.

It should be noted, that for the entire machine learning process in scenarios A to I (including scenario B-I) only the relative values (division) have been used. In the last scenario, which consists of the demonstration of the possible differentiation between the previous scenarios, only the absolute values have been used, since the main objective in this scenario is the distinction between them and not the similarity.

Figure 12 (a) shows the spectral composition of the impinging light at the surface of the retroreflective foil when only the LED of the VLS unit 2.0 is turned on.. Figure 12 (b) shows the spectral composition of the light provided by the laboratory fluorescent tubes once they reached a stable temperature. Figure 12 (c) shows the spectral distribution on the surface of the reflective foil of the merged light from the two sources of light previously mentioned. On the x axis the wavelength of the impinging light is shown and on the y axis the intensity of power measured.

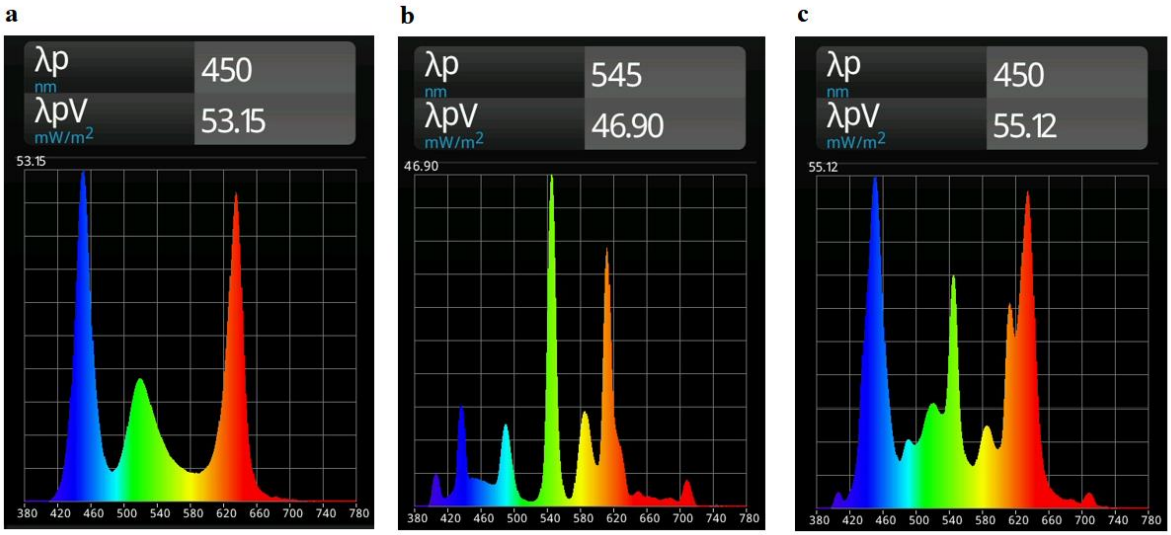

Figure 12 Spectral distribution of the impinging light on the retroreflective foil surface. (a) From only the LED. (b) From only the fluorescent tubes. (c) From the LED + fluorescent tubes.

2.1 Scenario A

In scenario A, the first configuration of retroreflective foils has been used, that is, the red and green configuration. Once all the data for the 20 runs have been obtained, using the GNU Octave software, the results have been represented graphically. In turn, for the machine learning process, the Orange data mining software [26] has been used to process the data obtained, through the KNN algorithm and obtain an error in degrees based on the prediction of the test data on the training database.

Table 3 summarizes the characteristics of Scenario A.

Table 3 **Scenario A**

Arm deviation	0º
Height of VLS unit 2.0 with respect to the robotic arm	1,2 m
Illumination	VLS unit 2.0 LED
Wristband	Red and green
Temperature of the LED	44.92 °C

Following the order discussed in the introduction, figure 13 shows the average absolute values of 500 values obtained for each angle of rotation of the robotic arm in the 1st run of scenario A, where the red and green wristband was used with only the LED as a source of light. On the x-axis all the rotation angles in which measurements have been taken are represented (from -175° to 175°), and on the y-axis in this case. the absolute value obtained by the photodiode in its three channels (red, green and blue) is shown.

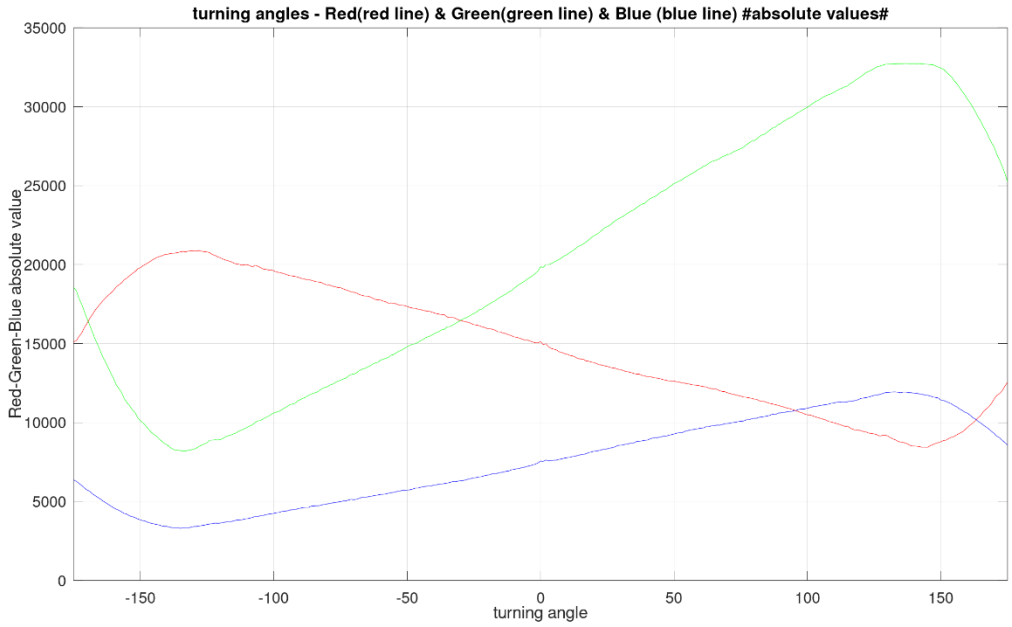

Figure 13 Absolute values taken from the 1st of the 20 measured runs in scenario A.

Figure 14 shows the relative values (subtraction) obtained from the values of figure 13. On the x axis all the rotation angles of the robotic arm are represented and on the y axis the relative value obtained from the subtraction of the absolute values as indicated in Table 1.

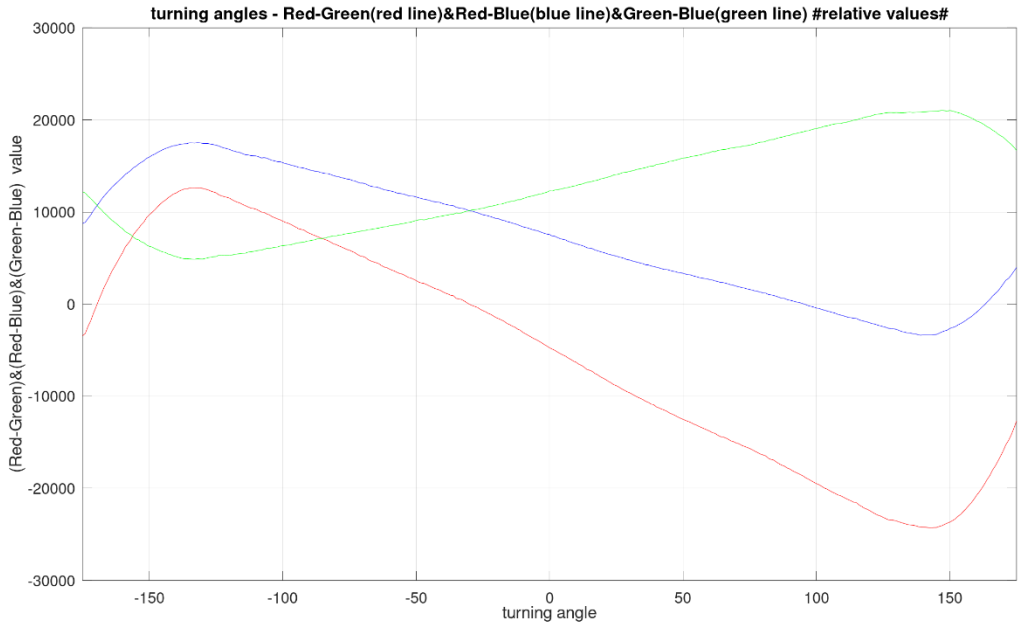

Figure 14 Subtraction relative values obtained from the absolute values from the 1st run of 20 in scenario A.

Figure 15 shows the relative values (division) obtained from the values of figure 13 following the same procedure as in the case of subtraction, but in this case the value obtained is given by the division of the absolute values, as it is indicated in table 1.

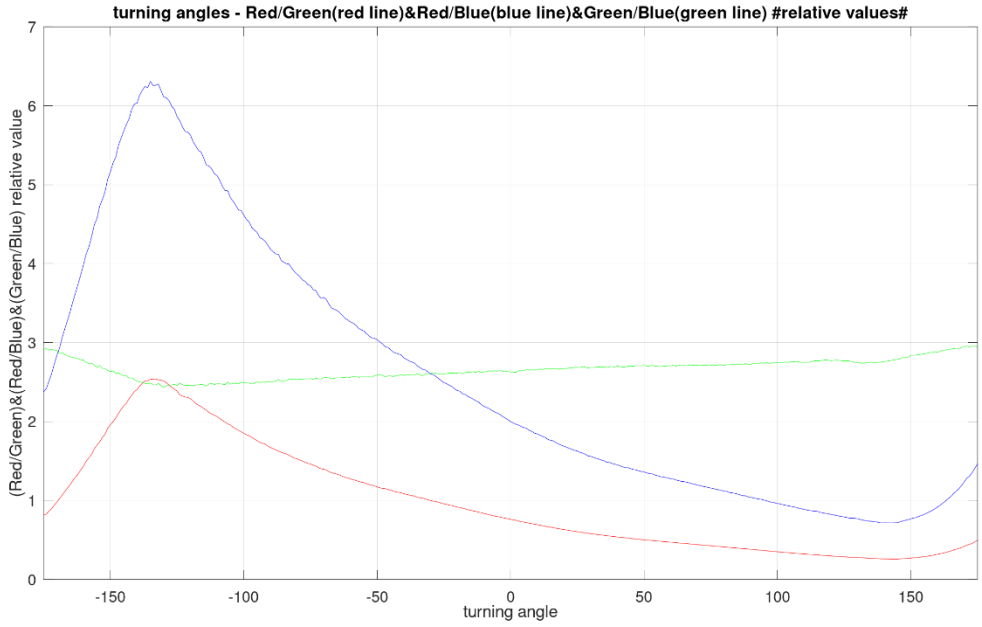

Figure 15 Division relative values obtained from the absolute values from the 1st run of 20 in scenario A.

Once the first 10 runs have been carried out as training database, the remaining 10 runs have been processed by the KNN algorithm as "test data" and the result of the prediction is shown in figure 16, where the x-axis is represented by all the rotation angles of the robotic arm, and the y-axis represents the predicted error at that same angle.

As commented at the beginning of the chapter, using only the relative values for the algorithm, the k value assigned in the algorithm has been 1, that is, for each value of the test database, the algorithm calculates the point within the training database with the shortest Euclidean distance, and that value is the one obtained at the output of the algorithm. Once this value is obtained, it is compared with the known actual rotation angle of the robotic arm (ground truth), subtracting both values to obtain the error in the prediction. This is how figure 16 shows the error in degrees with respect to the angle of rotation of the robotic arm.

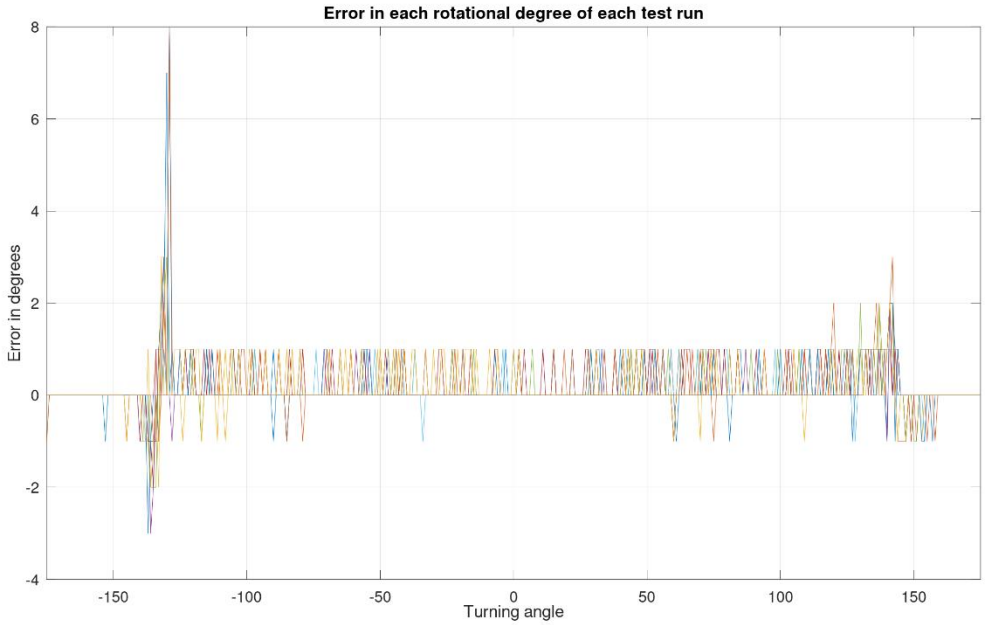

Figure 16 Error (given by: output of the KNN algorithm – Rotation degree tested) in each rotation degree of 10 test runs in scenario A.

2.2 Scenario B

Scenario B is a modification of scenario A, where instead of using the first configuration of reflective foils, the second (red, green and blue) has been used, which as already mentioned before, instead of using two colours, uses three colours, red, green and blue.

Table 4 summarizes the characteristics of Scenario B.

Table 4 **Scenario B**

Arm deviation	0º
Height of VLS unit 2.0 with respect to the robotic arm	1,2 m
Illumination	VLS unit 2.0 LED
Wristband	Red, green and blue
Temperature of the LED	44.90 °C

Following the same procedure as in the previous scenario, figure 17 shows the absolute values obtained during the first of the 20 runs.

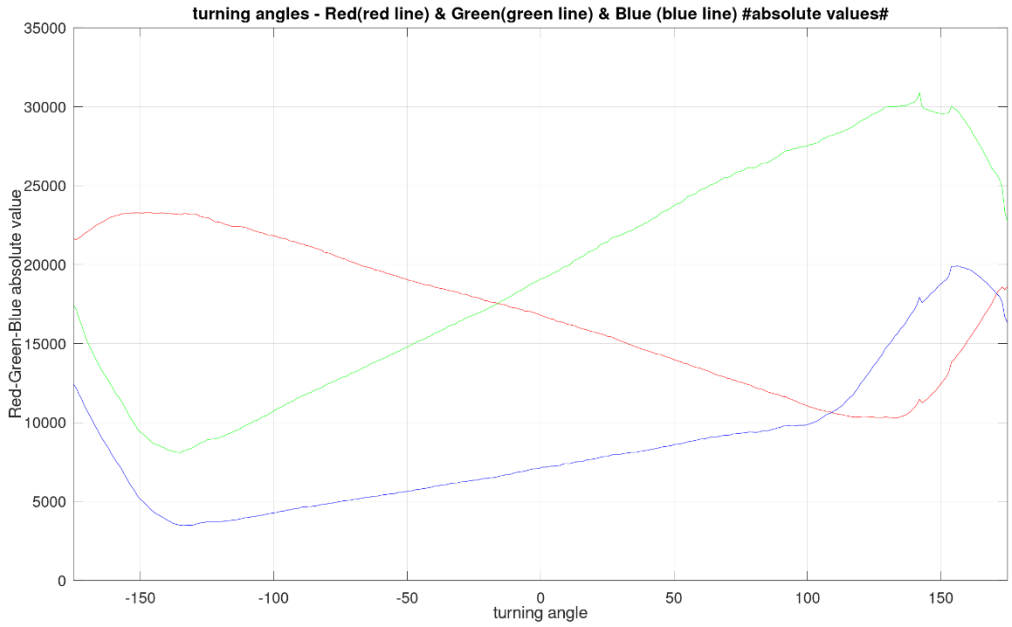

Figure 17 Absolute values taken from the 1st of the 20 measured runs in scenario B.

The following figure (figure 18) shows the relative values (subtraction) obtained for this scenario.

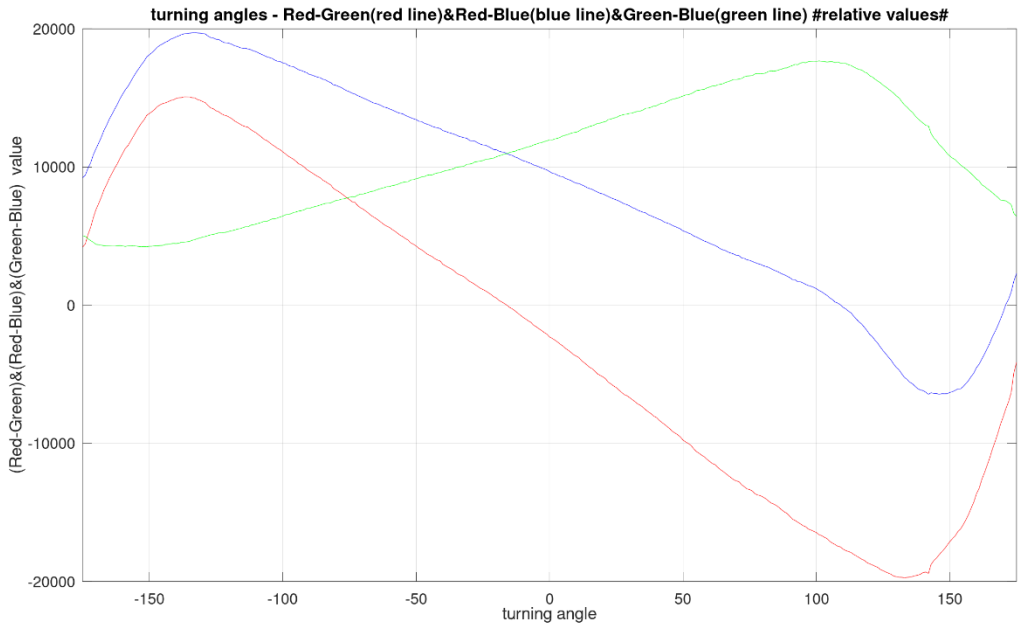

Figure 18 Subtraction relative values obtained from the absolute values from the 1st run of 20 in scenario B.

The following figure (figure 19) shows the relative values (division) obtained for this scenario.

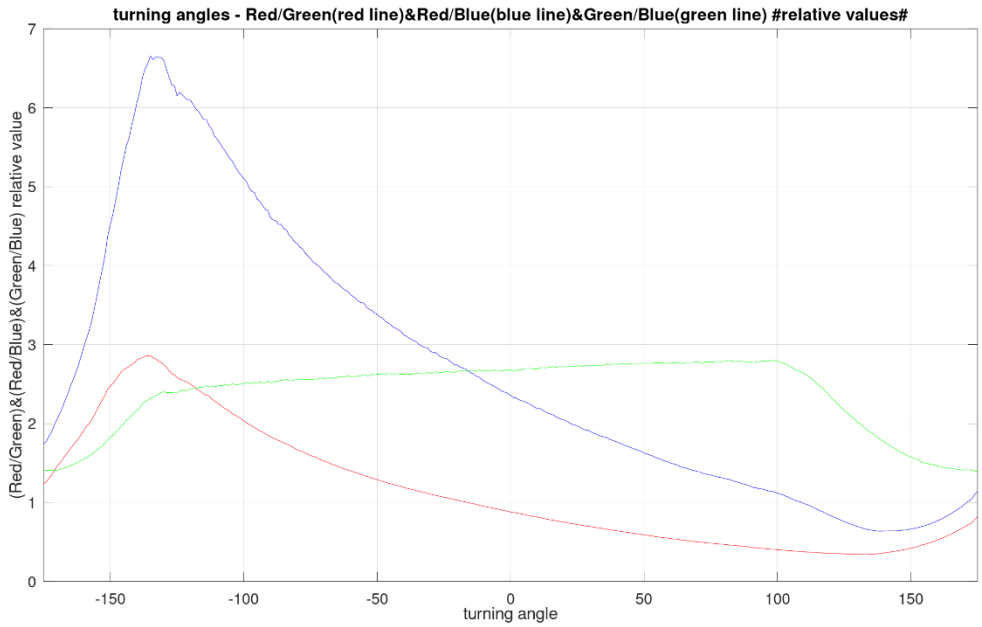

Figure 19 Division relative values obtained from the absolute values from the 1st run of 20 in scenario B.

Following the same steps as in scenario A, the error obtained for this scenario is the one shown in figure 20.

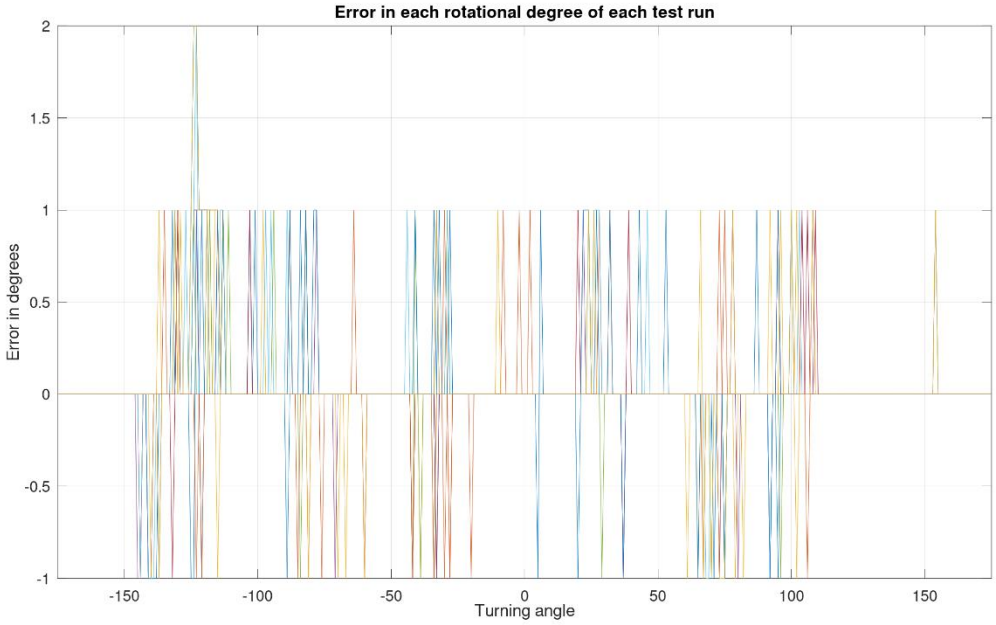

Figure 20 Error (given by: output of the KNN algorithm – Rotation degree tested) in each rotation degree of 10 test runs in scenario B.

2.3 Scenario C

Scenario C is a modification of scenario B, where the robotic arm has been moved + 5º in the vertical axis.

Table 5 summarizes the characteristics of Scenario C.

Table 5 **Scenario C**

Arm deviation	Tilt + 5º
Height of VLS unit 2.0 with respect to the robotic arm	1,2 m
Illumination	VLS unit 2.0 LED
Wristband	Red, green and blue
Temperature of the LED	45.13 ºC

Following the procedure, the absolute values obtained are those shown in figure 21.

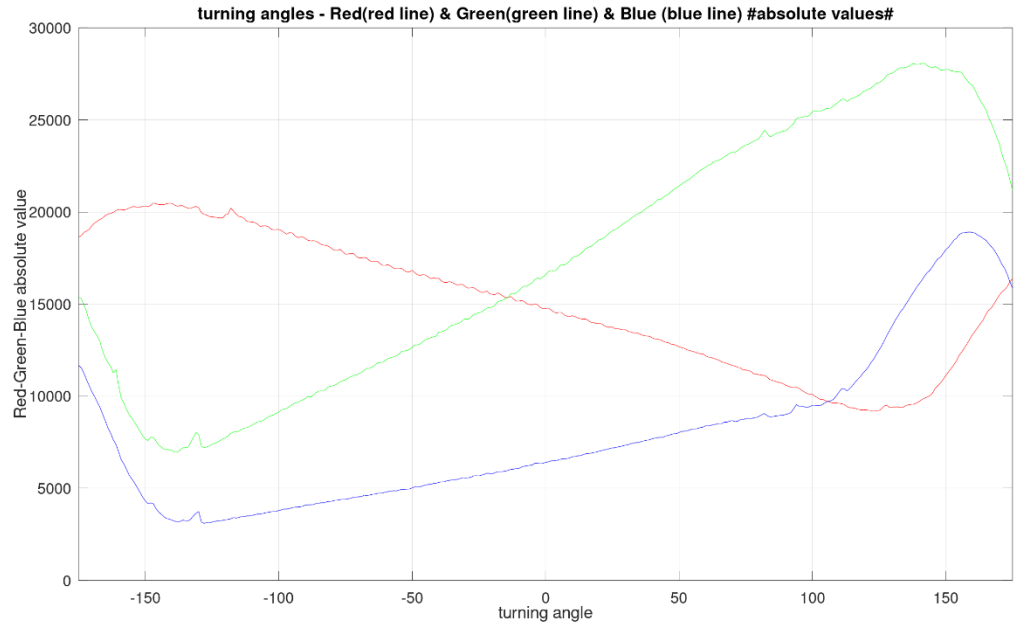

Figure 21 Absolute values taken from the 1st of the 20 measured runs in scenario C.

The subtraction relative values obtained are those shown in figure 22.

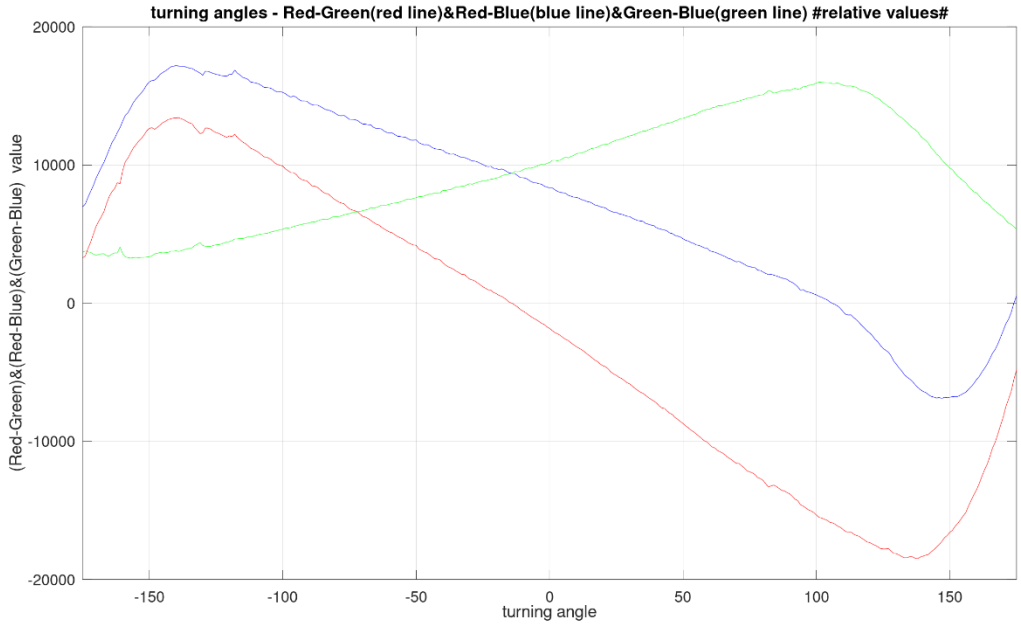

Figure 22 Subtraction relative values obtained from the absolute values from the 1st run of 20 in scenario C.

The division relative values obtained are those shown in figure 23.

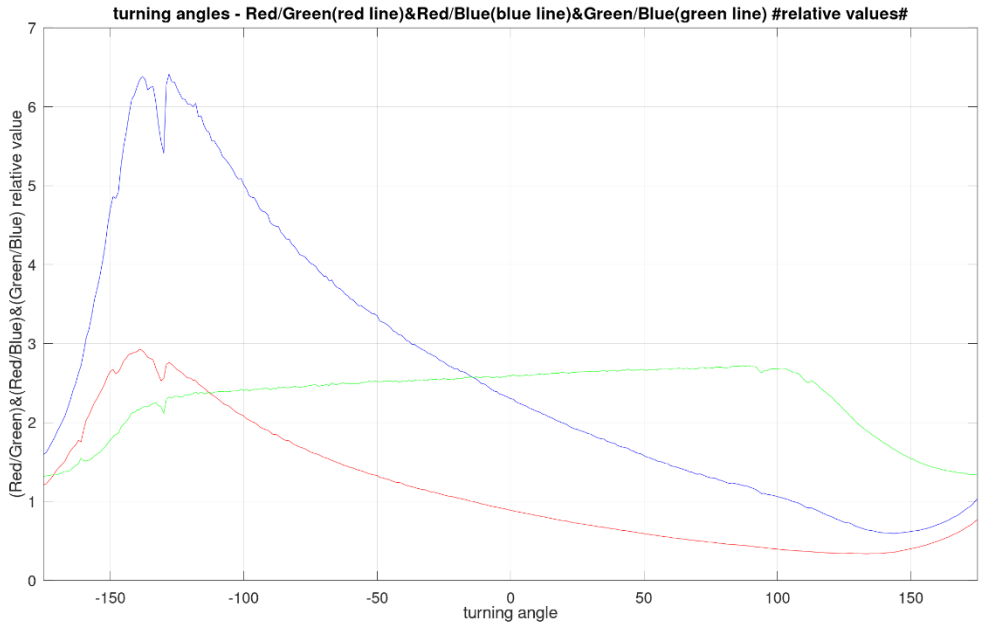

Figure 23 Division relative values obtained from the absolute values from the 1st run of 20 in scenario C.

The error in degrees obtained is the one shown in figure 24.

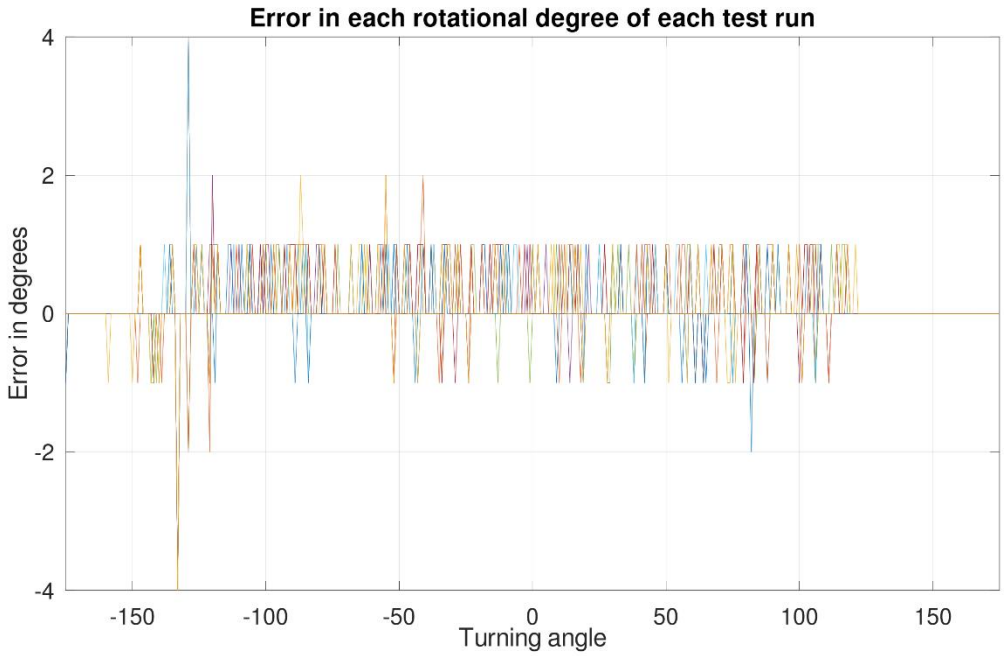

Figure 24 Error (given by: output of the KNN algorithm – Rotation degree tested) in each rotation degree of 10 test runs in scenario C.

2.4 Scenario D

Scenario D is a modification of scenario A, where the robotic arm has been moved + 10º in the vertical axis.

Table 6 summarizes the characteristics of Scenario D.

Table 6 **Scenario D**

Arm deviation	Tilt + 10º
Height of VLS unit 2.0 with respect to the robotic arm	1,2 m
Illumination	VLS unit 2.0 LED
Wristband	Red, green and blue
Temperature of the LED	45.28 °C

Following the procedure, the absolute values obtained are those shown in figure 25.

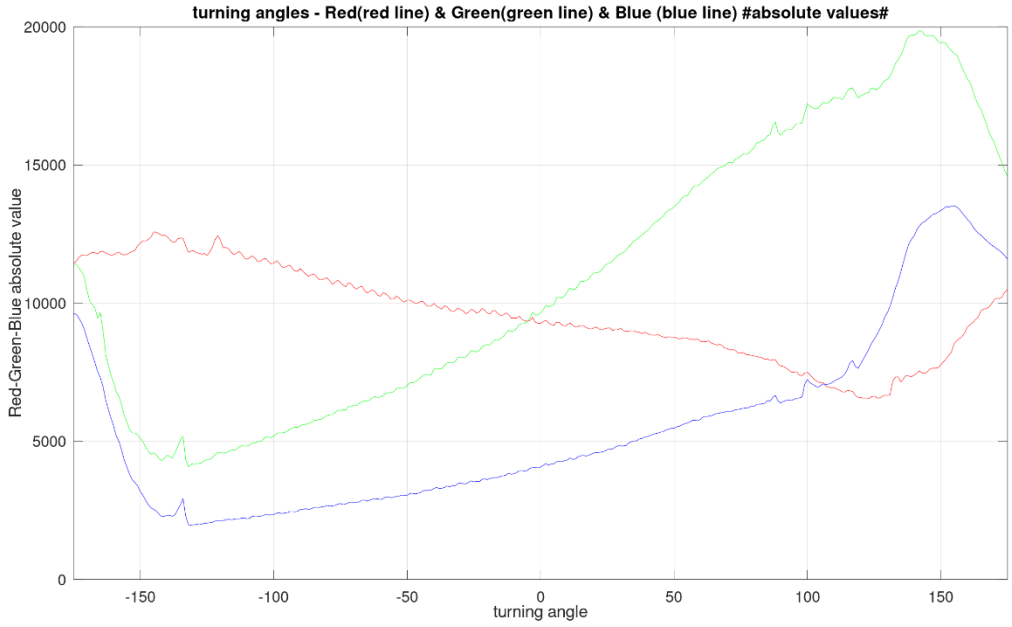

Figure 25 Absolute values taken from the 1st of the 20 measured runs in scenario D.

The subtraction relative values obtained are those shown in figure 26.

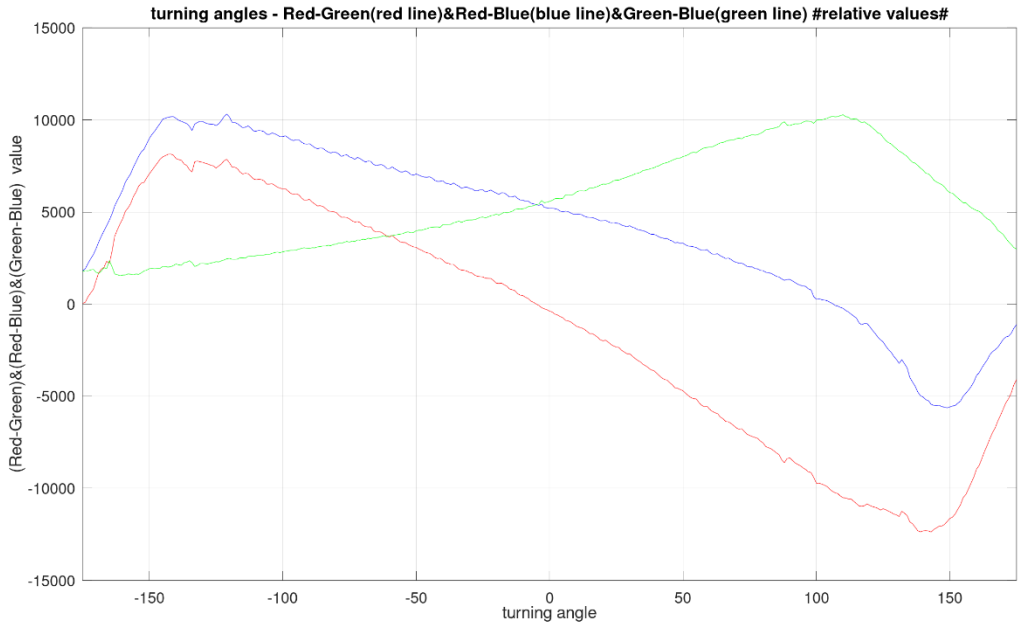

Figure 26 Subtraction relative values obtained from the absolute values from the 1st run of 20 in scenario D.

The division relative values obtained are those shown in figure 27.

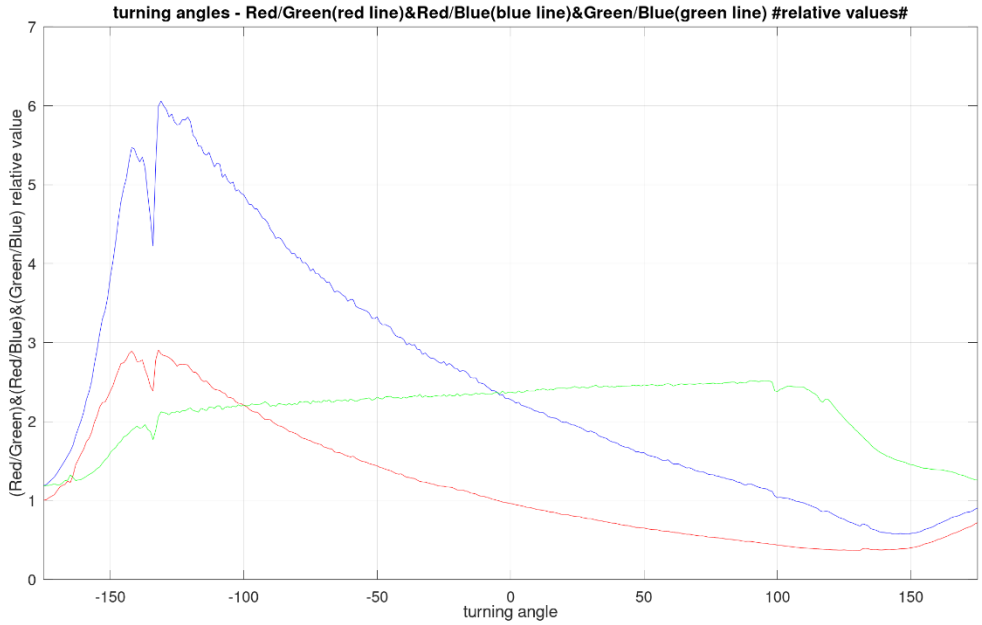

Figure 27 Division relative values obtained from the absolute values from the 1st run of 20 in scenario D.

The error in degrees obtained is the one shown in figure 28.

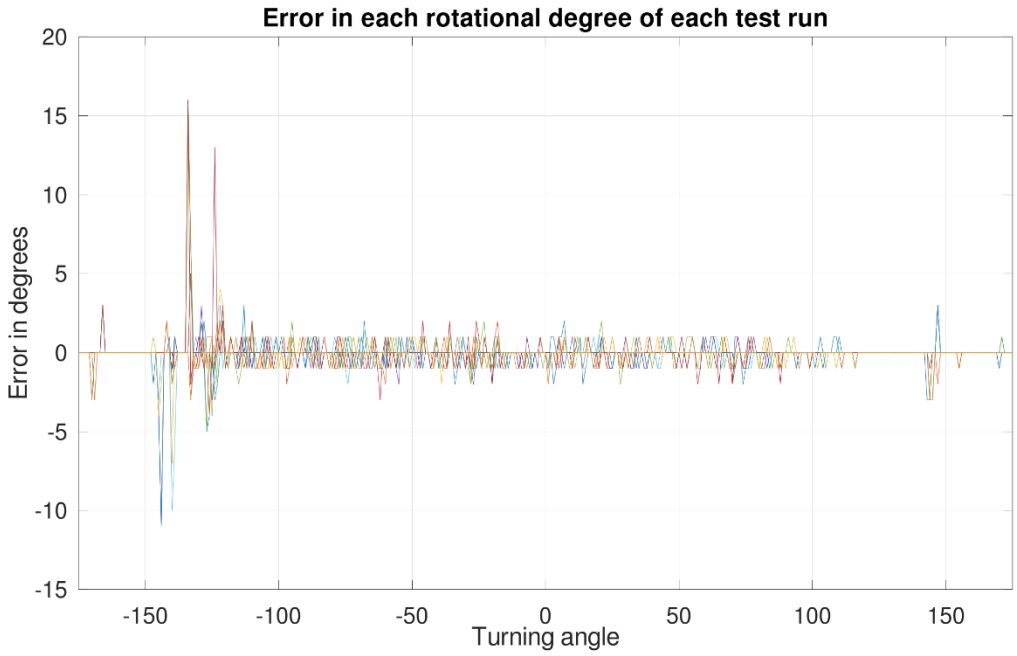

Figure 28 Error (given by: output of the KNN algorithm – Rotation degree tested) in each rotation degree of 10 test runs in scenario D.

2.5 Scenario E

Scenario E is a modification of scenario B, where the robotic arm has been moved -5º in the vertical axis.

Table 7 summarizes the characteristics of Scenario E.

Table 7 **Scenario E**

Arm deviation	Tilt - 5º
Height of VLS unit 2.0 with respect to the robotic arm	1,2 m
Illumination	VLS unit 2.0 LED
Wristband	Red, green and blue
Temperature of the LED	45.11 °C

Following the procedure, the absolute values obtained are those shown in figure 29.

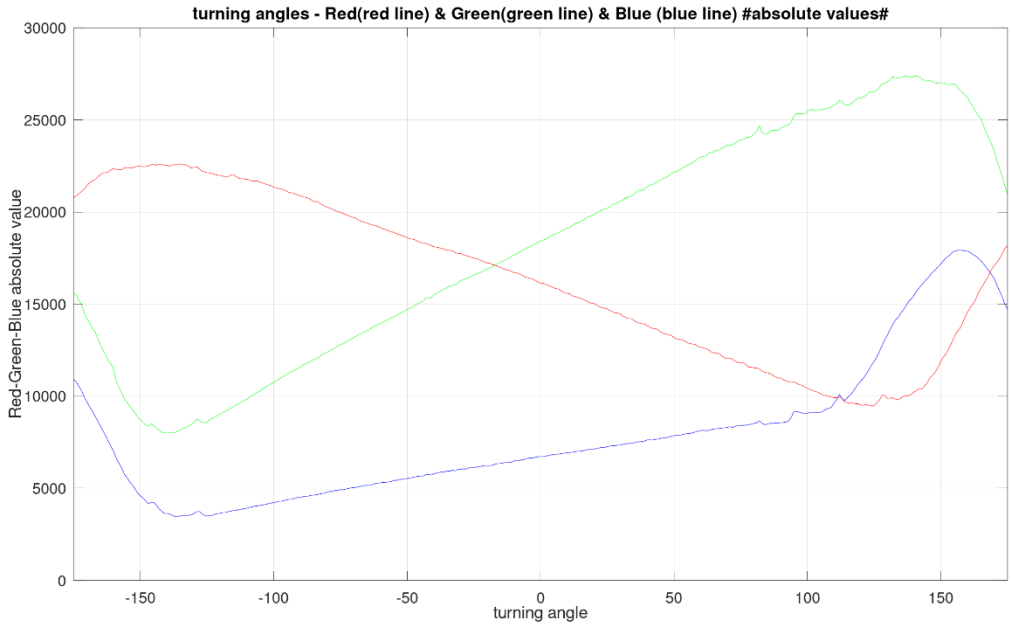

Figure 29 Absolute values taken from the 1st of the 20 measured runs in scenario E.

The subtraction relative values obtained are those shown in figure 30.

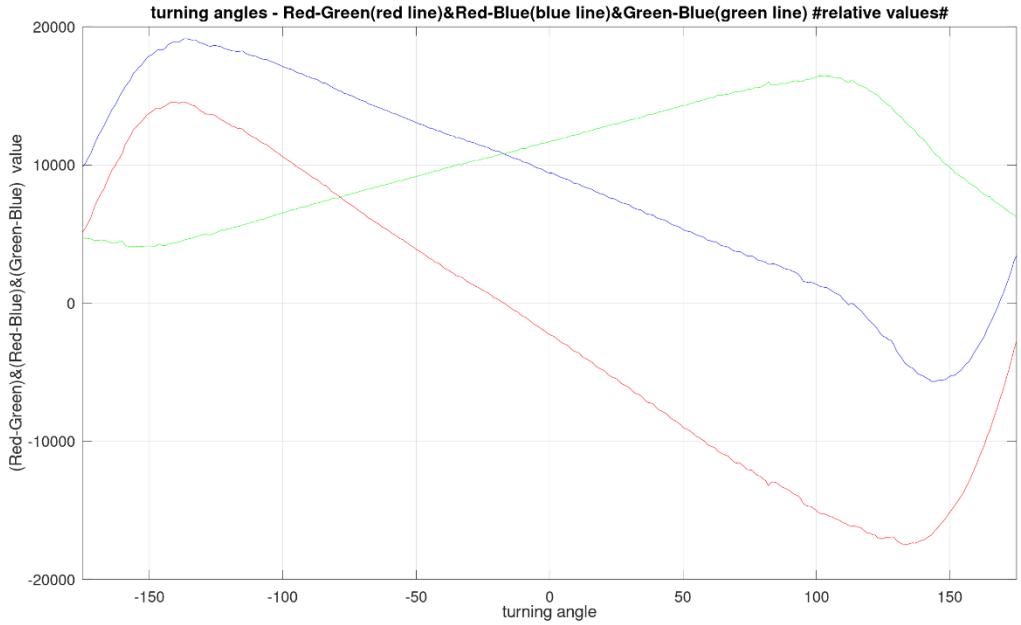

Figure 30 Subtraction relative values obtained from the absolute values from the 1st run of 20 in scenario E.

The division relative values obtained are those shown in figure 31.

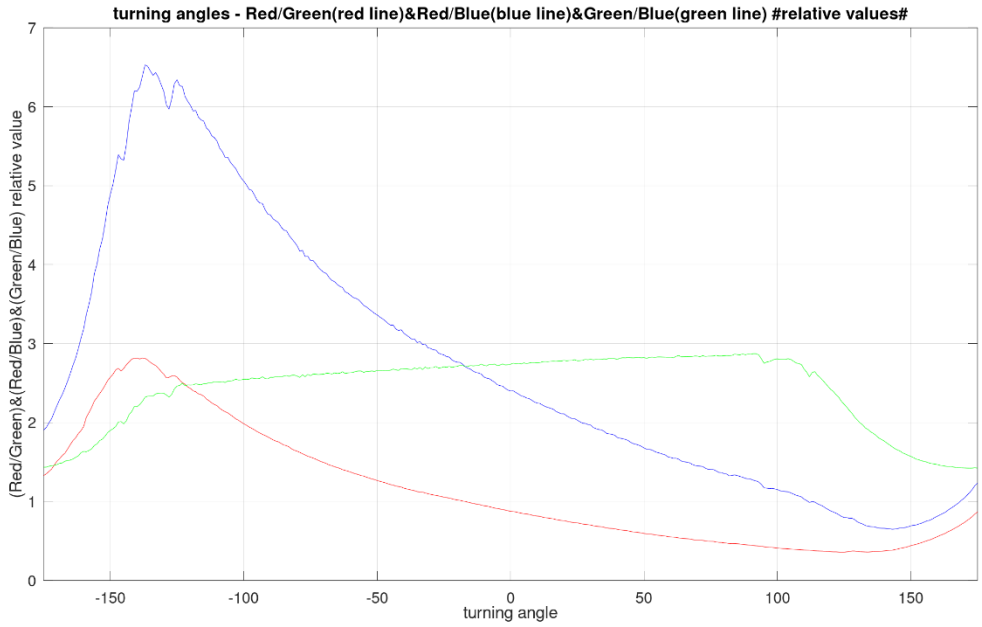

Figure 31 Division relative values obtained from the absolute values from the 1st run of 20 in scenario E.

The error in degrees obtained is the one shown in figure 32.

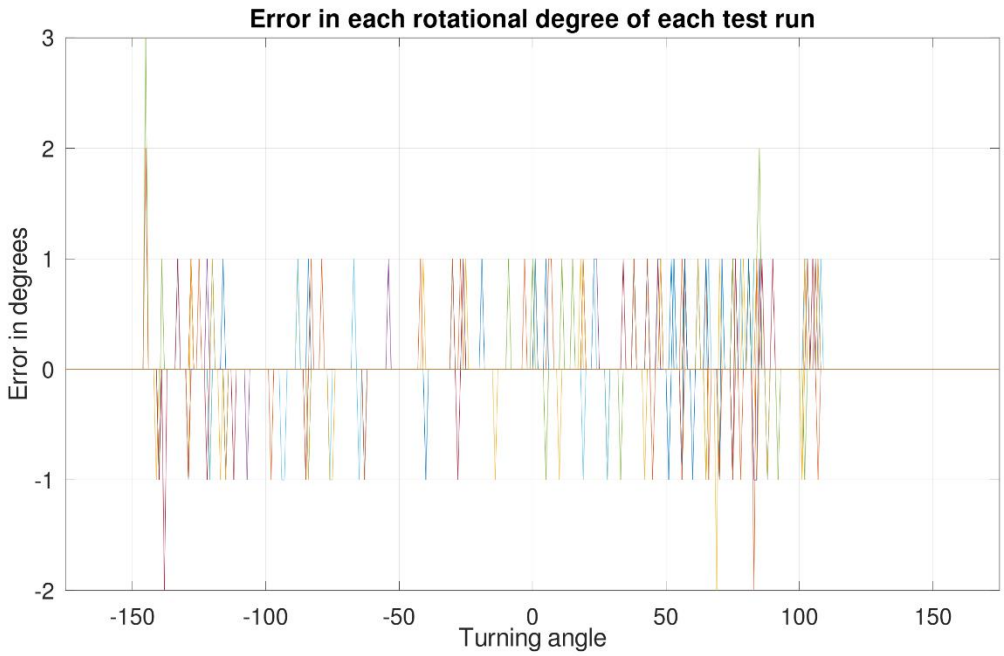

Figure 32 Error (given by: output of the KNN algorithm – Rotation degree tested) in each rotation degree of 10 test runs in scenario E.

2.6 Scenario F

Scenario F is a modification of scenario B, where the robotic arm has been moved -10º in the vertical axis.

Table 8 summarizes the characteristics of Scenario F.

Table 8 **Scenario F**

Arm deviation	Tilt - 10º
Height of VLS unit 2.0 with respect to the robotic arm	1,2 m
Illumination	VLS unit 2.0 LED
Wristband	Red, green and blue
Temperature of the LED	45.37 °C

Following the procedure, the absolute values obtained are those shown in figure 33.

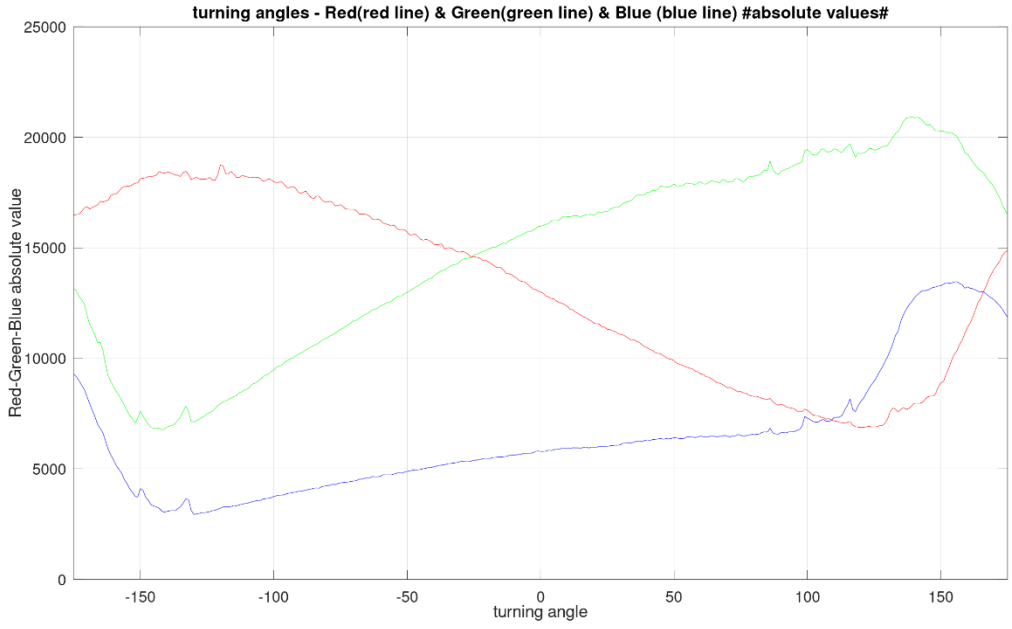

Figure 33 Absolute values taken from the 1st of the 20 measured runs in scenario F.

The subtraction relative values obtained are those shown in figure 34.

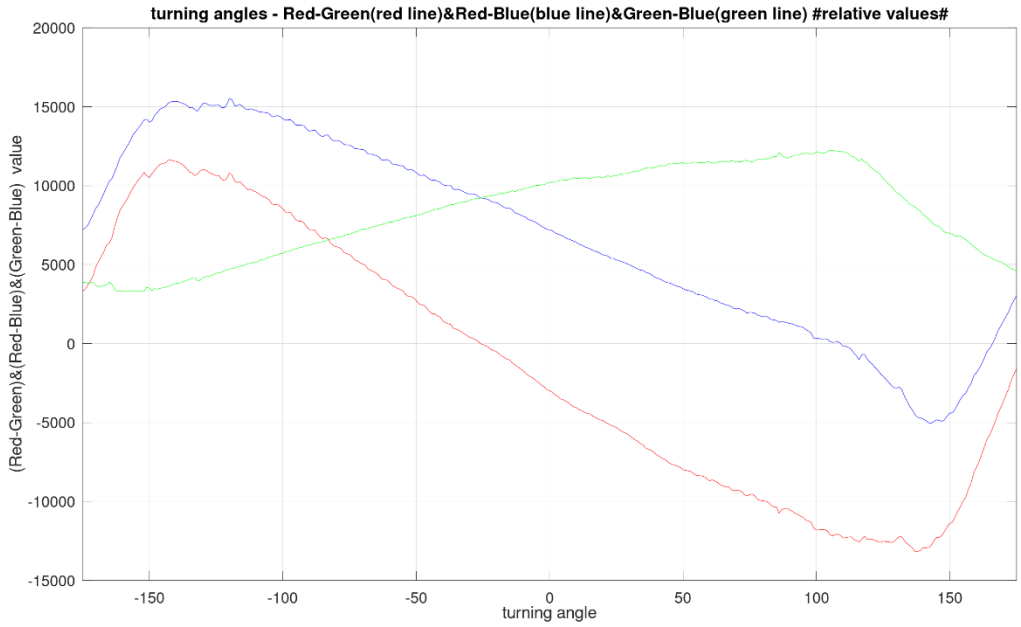

Figure 34 Subtraction relative values obtained from the absolute values from the 1st run of 20 in scenario F.

The division relative values obtained are those shown in figure 35.

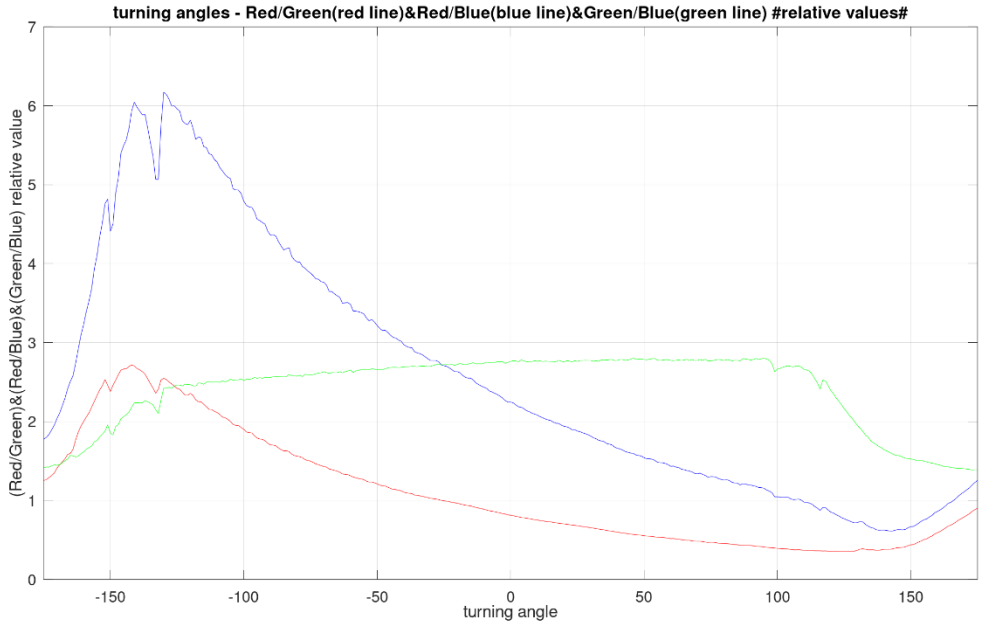

Figure 35 Division relative values obtained from the absolute values from the 1st run of 20 in scenario F.

The error in degrees obtained is the one shown in figure 36.

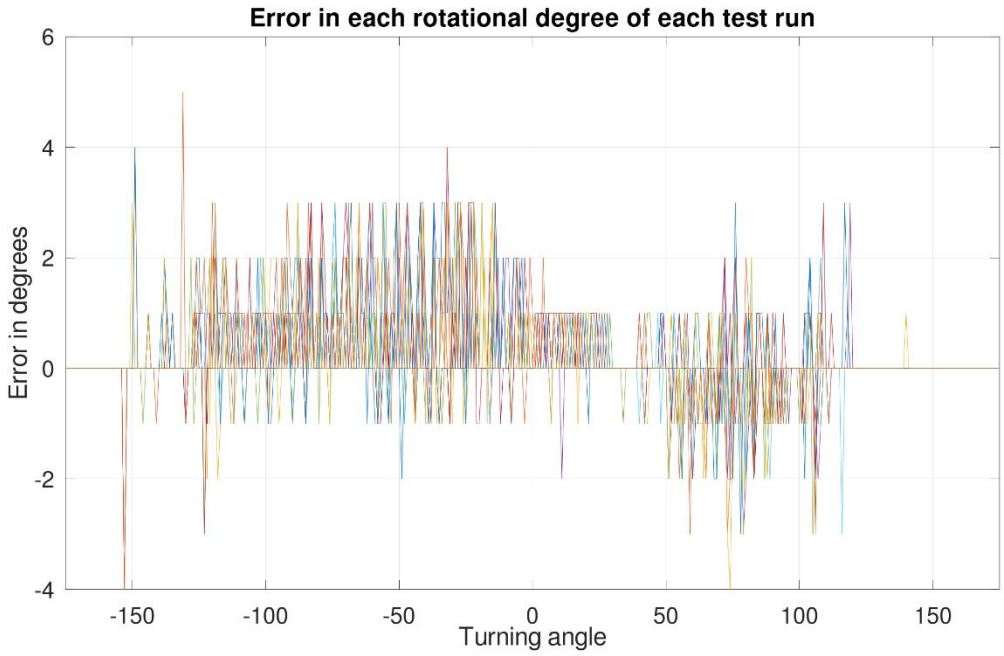

Figure 36 Error (given by: output of the KNN algorithm – Rotation degree tested) in each rotation degree of 10 test runs in scenario F.

2.7 Scenario G

Scenario G is a modification of scenario B, where the robotic arm has been moved +5º in the horizontal axis.

Table 9 summarizes the characteristics of Scenario G.

Table 9 **Scenario G**

Arm deviation	Azimuth + 5º
Height of VLS unit 2.0 with respect to the robotic arm	1,2 m
Illumination	VLS unit 2.0 LED
Wristband	Red, green and blue
Temperature of the LED	44.95 °C

Following the procedure, the absolute values obtained are those shown in figure 37.

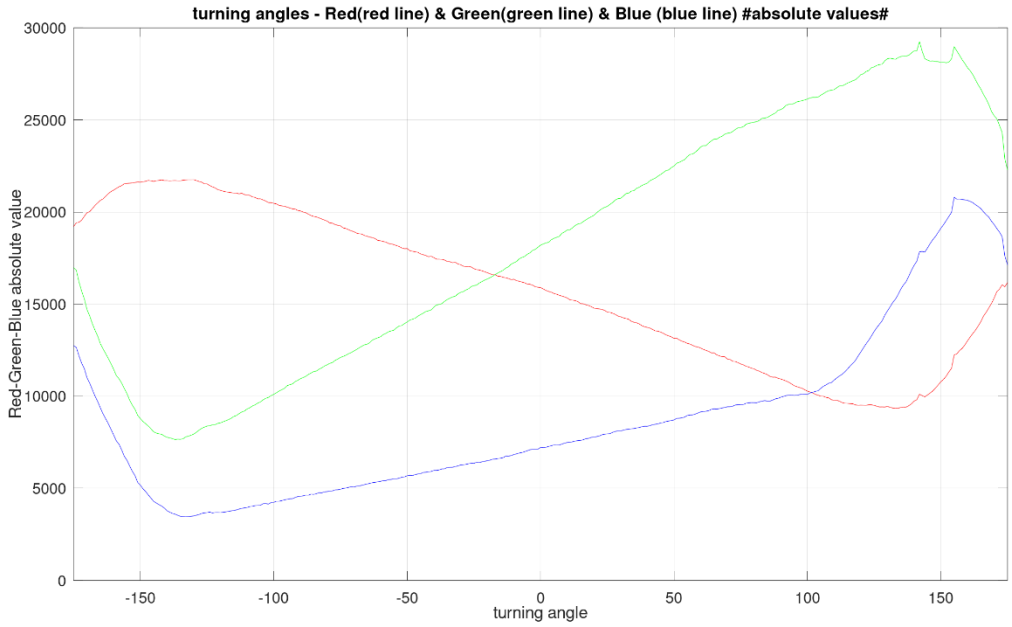

Figure 37 Absolute values taken from the 1st of the 20 measured runs in scenario G.

The subtraction relative values obtained are those shown in figure 38.

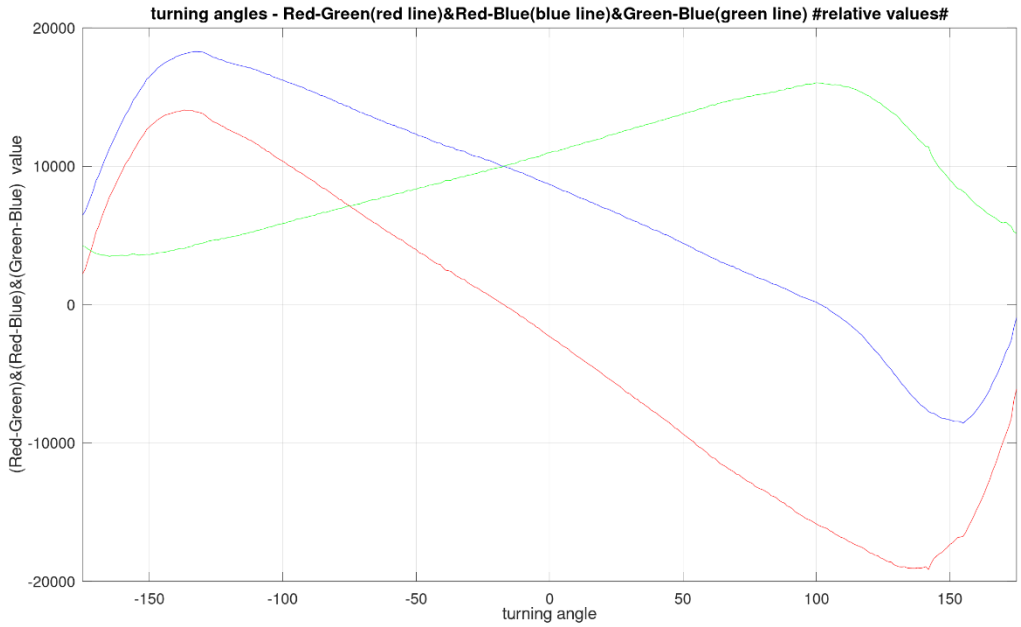

Figure 38 Subtraction relative values obtained from the absolute values from the 1st run of 20 in scenario G.

The division relative values obtained are those shown in figure 39.

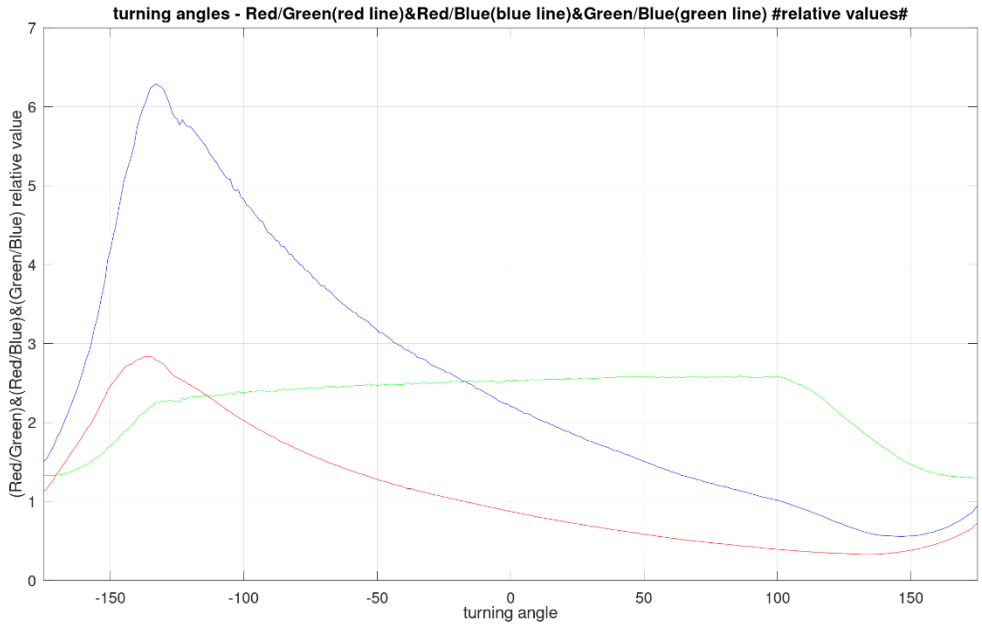

Figure 39 Division relative values obtained from the absolute values from the 1st run of 20 in scenario G.

The error in degrees obtained is the one shown in figure 40.

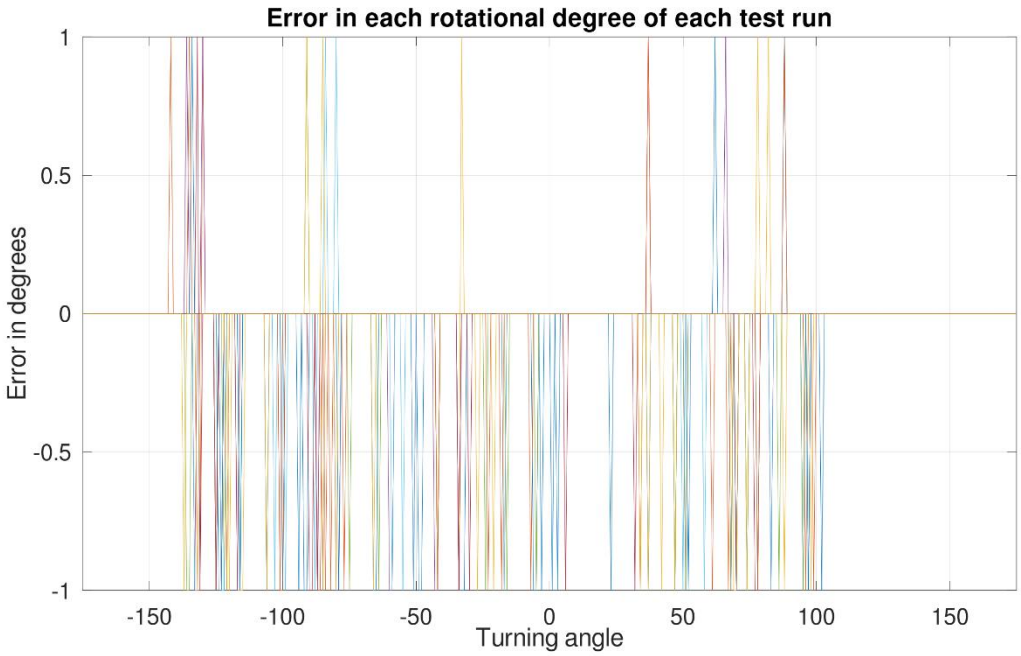

Figure 40 Error (given by: output of the KNN algorithm – Rotation degree tested) in each rotation degree of 10 test runs in scenario G.

2.8 Scenario H

Scenario G is a modification of scenario B, where the robotic arm has been moved -5º in the horizontal axis.

Table 10 summarizes the characteristics of Scenario H.

Table 10 **Scenario H**

Arm deviation	Azimuth - 5º
Height of VLS unit 2.0 with respect to the robotic arm	1,2 m
Illumination	VLS unit 2.0 LED
Wristband	Red, green and blue
Temperature of the LED	45.52 °C

Following the procedure, the absolute values obtained are those shown in figure 41.

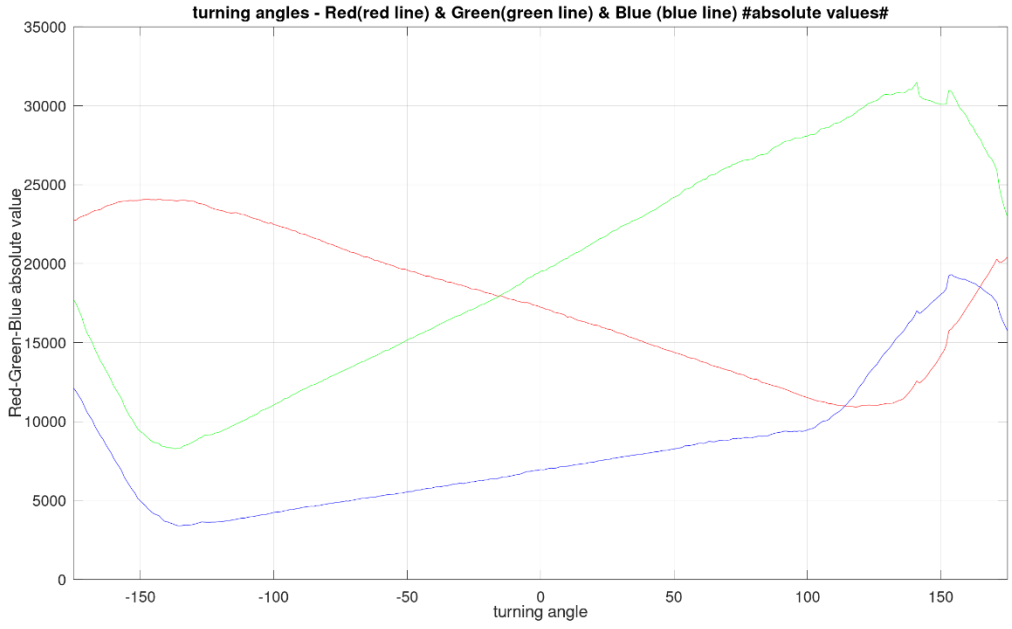

Figure 41 Absolute values taken from the 1st of the 20 measured runs in scenario H.

The subtraction relative values obtained are those shown in figure 42.

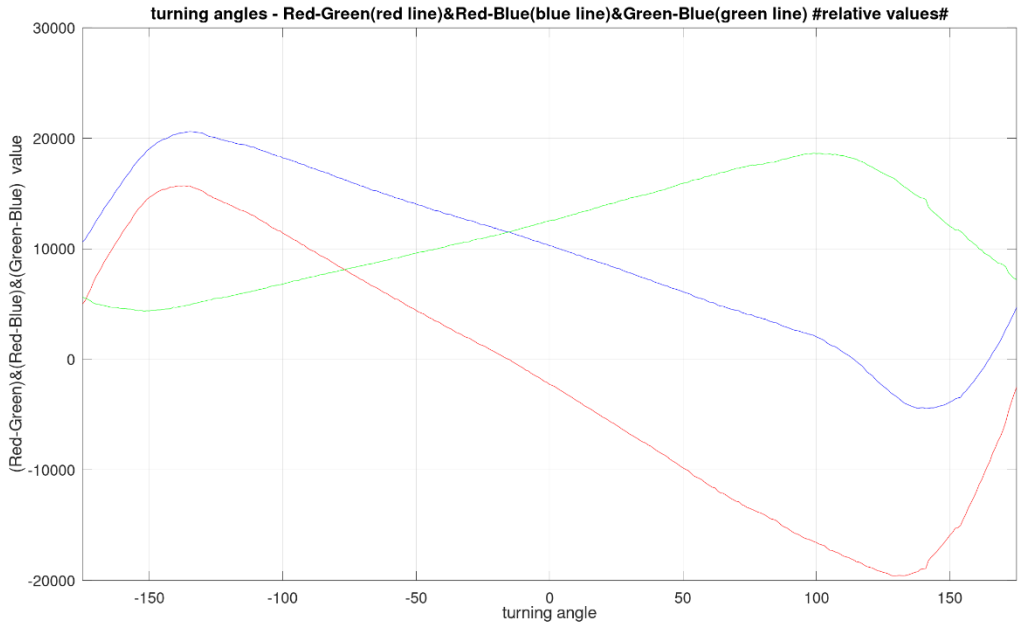

Figure 42 Subtraction relative values obtained from the absolute values from the 1st run of 20 in scenario H.

The division relative values obtained are those shown in figure 43.

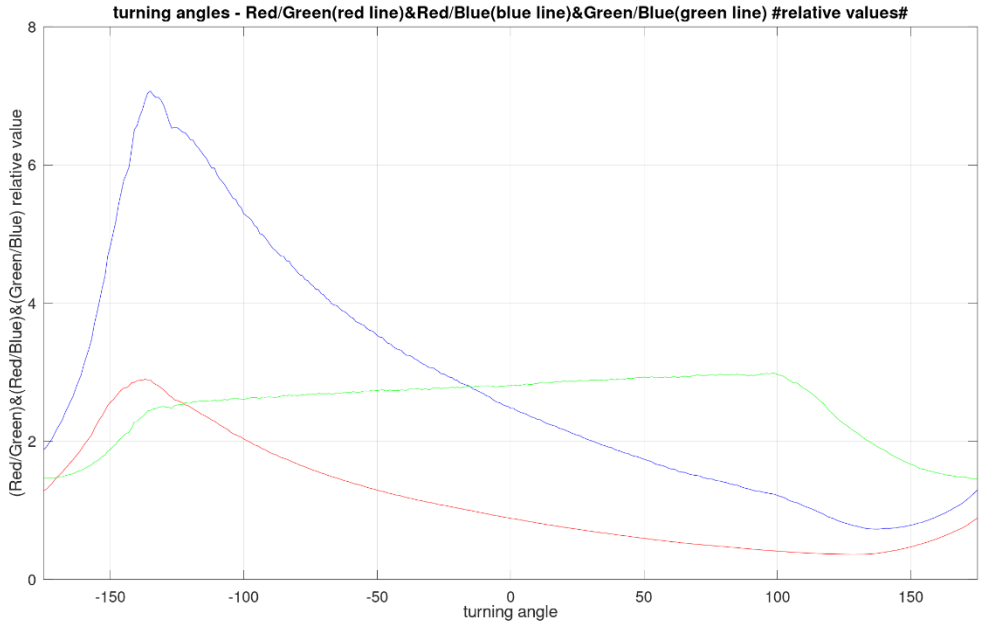

Figure 43 Division relative values obtained from the absolute values from the 1st run of 20 in scenario H.

The error in degrees obtained is the one shown in figure 44.

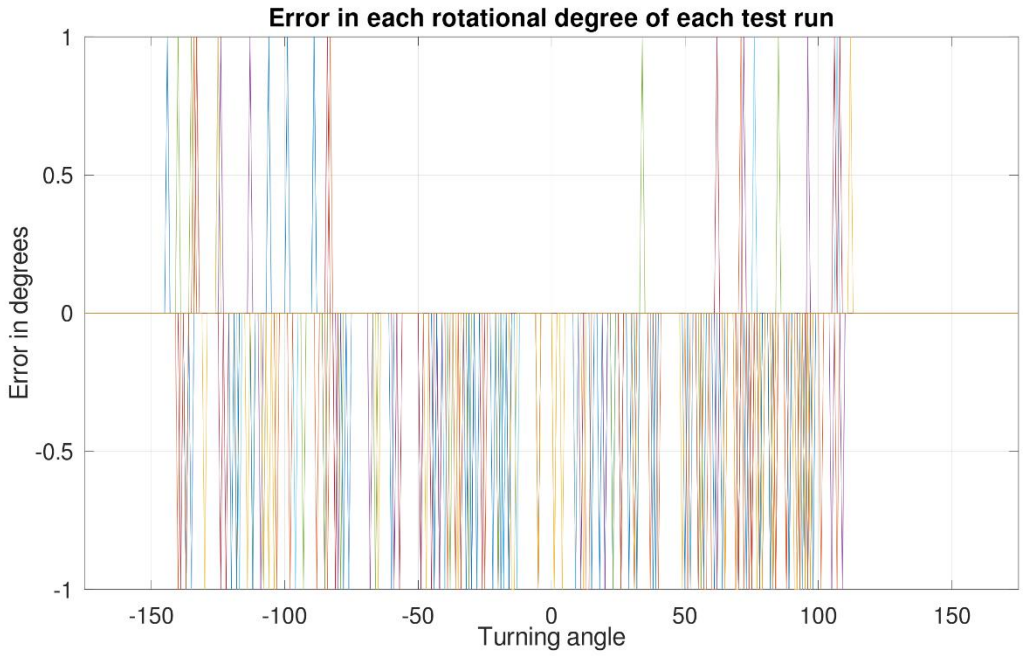

Figure 44 Error (given by: output of the KNN algorithm – Rotation degree tested) in each rotation degree of 10 test runs in scenario H.

2.9 Scenario I

The data and results obtained in scenario I follow the same procedure as the previous scenarios, with the only difference that instead of not only using the LED of the VLS unit 2.0, the room lights have also been turned on. The following table (table 11) shows the characteristics of the current scenario.

Table 11 **Scenario I**

Arm deviation	0º
Height of VLS unit 2.0 with respect to the robotic arm	1,2 m
Illumination	VLS unit 2.0 LED + Ambient light
Wristband	Red, green and blue
Temperature of the LED	45.38 °C

Following the procedure, the absolute values obtained are those shown in figure 45.

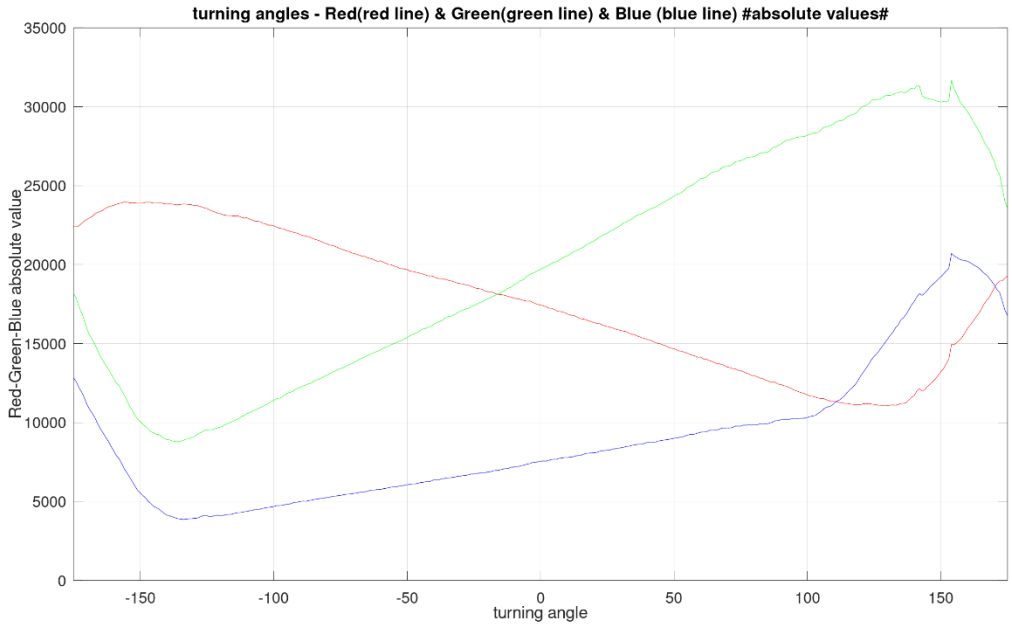

Figure 45 Absolute values taken from the 1st of the 20 measured runs in scenario I.

The subtraction relative values obtained are those shown in figure 46.

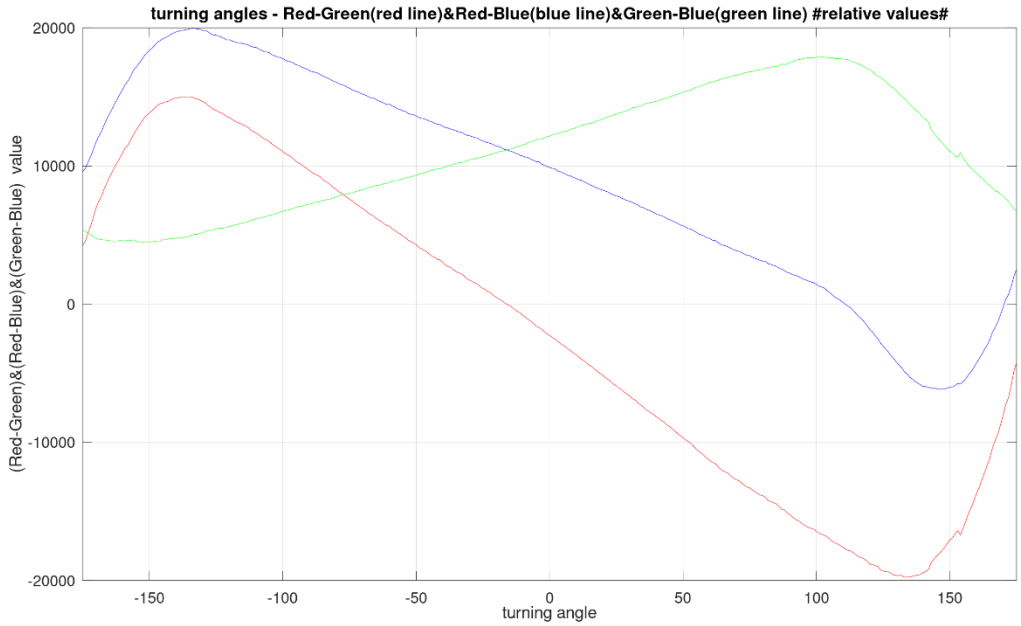

Figure 46 Subtraction relative values obtained from the absolute values from the 1st run of 20 in scenario I.

The division relative values obtained are those shown in figure 47.

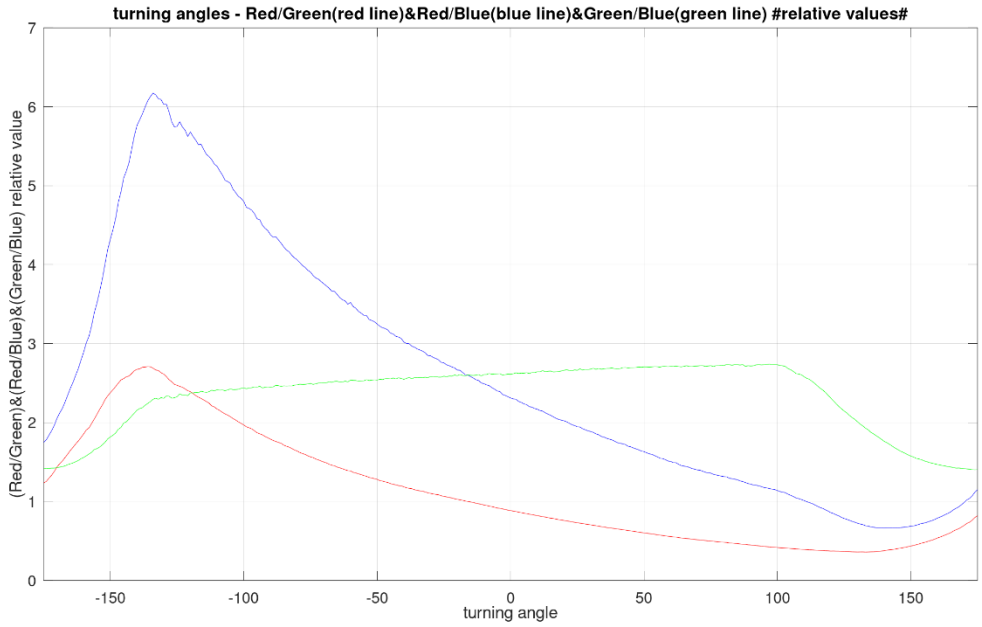

Figure 47 Division relative values obtained from the absolute values from the 1st run of 20 in scenario I.

The error in degrees obtained is the one shown in figure 48.

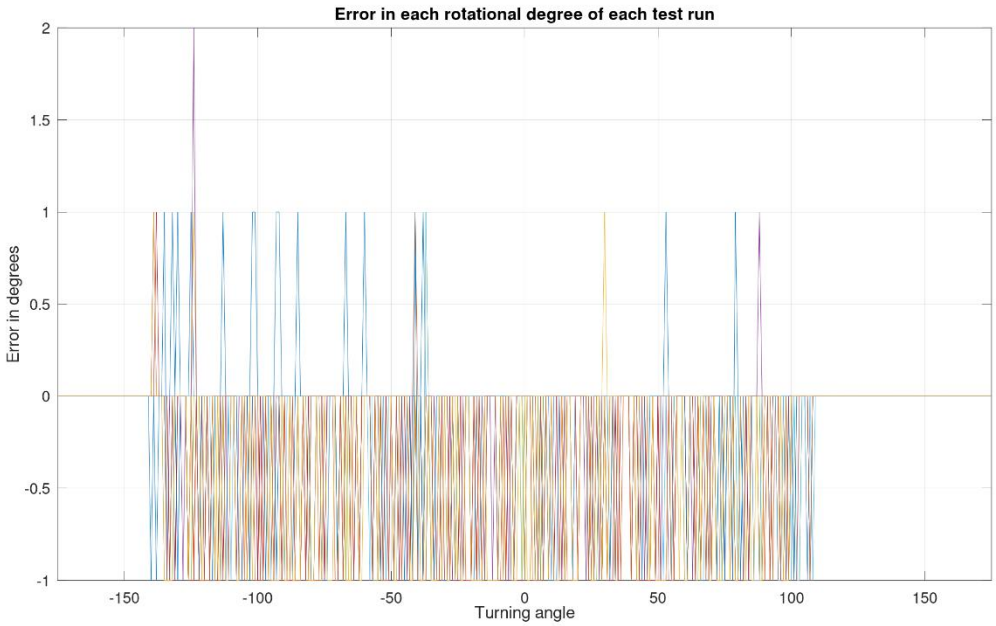

Figure 48 Error (given by: output of the KNN algorithm – Rotation degree tested) in each rotation degree of 10 test runs in scenario I.

2.10 Scenario B - I

In the following scenario, we intend to show the effect of adding a new light source to our prediction system for the rotation angle of the robotic arm. For this, the algorithm has been trained in the same way as in scenario B, where the light source was only the LED, but at the time of testing, the data from scenario I was used, where both light sources, the LED of the VLS unit 2.0 as well as the ambient light of the room was turned on..

Figure 49 shows the differences in the absolute values of the 1st run for each scenario, where the solid line shows the absolute values for scenario B, while the dashed line shows the absolute values for scenario I.

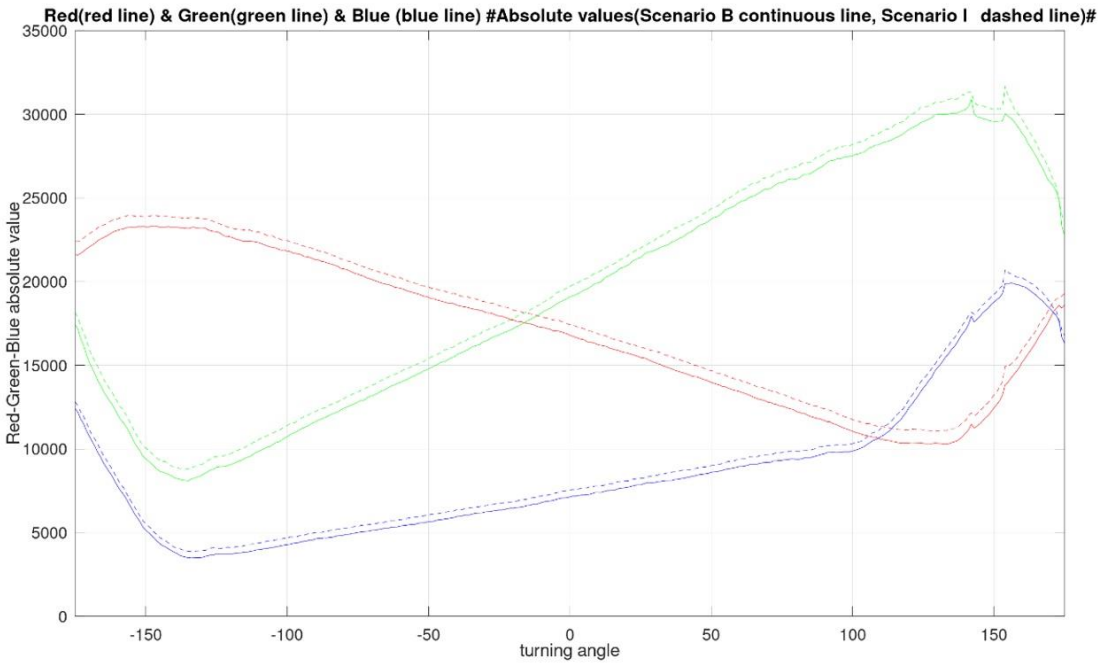

Figure 49 Absolute values taken from the 1st of the 20 measured runs, Continuous line represents scenario B. Dashed line represents scenario I.

In the same way, we can represent the relative values for the subtraction and division of the absolute values in figure 50 and in figure 51 respectively.

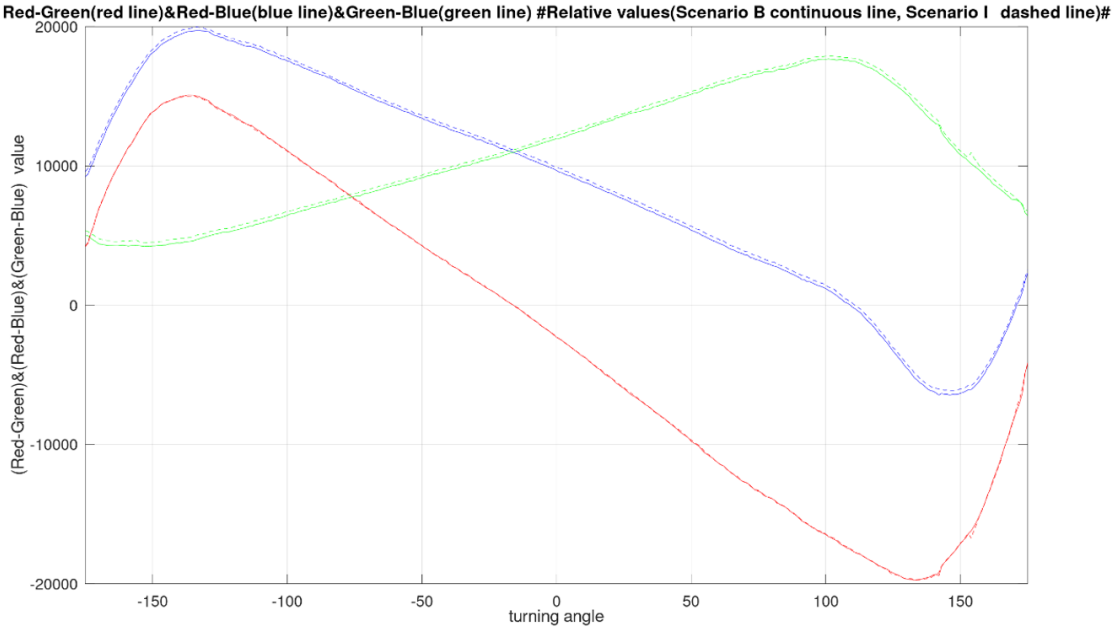

Figure 50 Subtraction relative values obtained from the absolute values from the 1st run of 20, Continuous line represents scenario B. Dashed line represents scenario I.

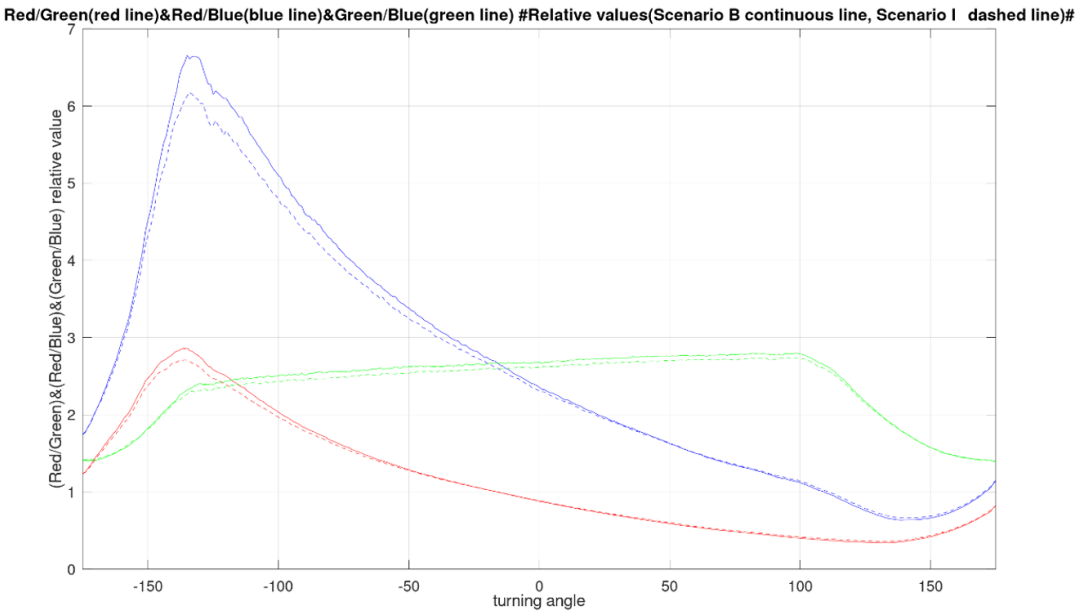

Figure 51 Division relative values obtained from the absolute values from the 1st run of 20, Continuous line represents scenario B. Dashed line represents scenario I.

Figure 52 shows the error value obtained from the prediction of the algorithm, which, as mentioned above, has been trained and tested in two different scenarios.

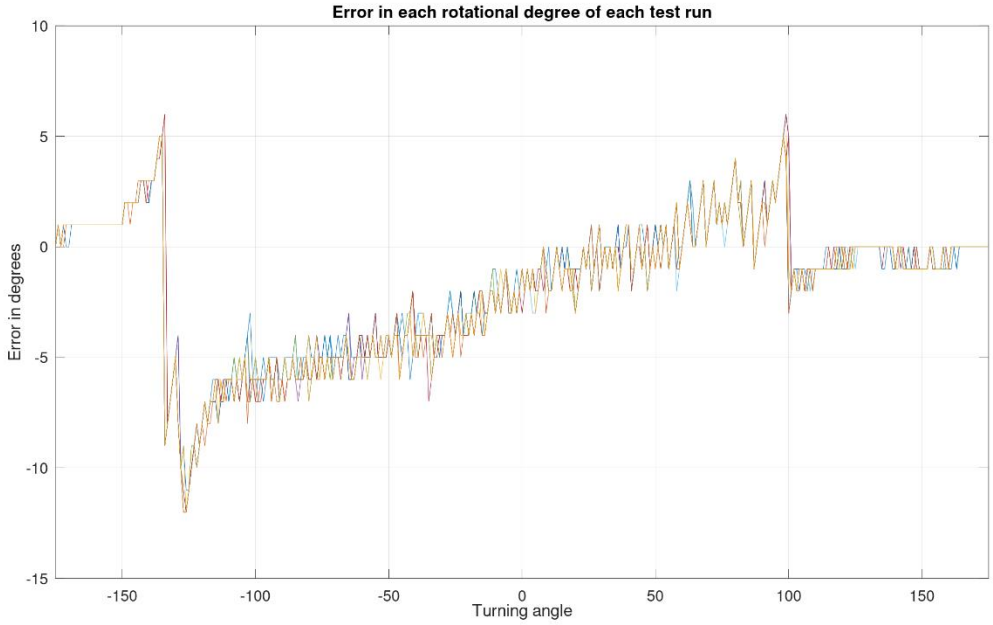

Figure 52 Error (given by: output of the KNN algorithm – Rotation degree tested) in each rotation degree of 10 test runs in scenario I, using as a training data 10 runs from scenario B.

2.11 Overall scenario

The main reason for this section is the distinction between the previous scenarios (B to I) by using the same KNN algorithm used previously. To do so, as commented at the beginning of this chapter, only absolute values will be used. That is, all the data obtained for training in each scenario have been combined to be used as a database, in turn, for testing, all the data from all the scenarios have been combined. With this procedure, it has been possible to obtain the Table 12 where the percentage of prediction of each value tested in each scenario is shown.

Table 12 Predicted values from scenario to scenario

	Scenario B	Scenario C	Scenario D	Scenario E	Scenario F	Scenario G	Scenario H	Scenario I	Num. of values
Scenario B	100%	0,00%	0,00%	0,00%	0,00%	0,00%	0,00%	0,40%	3510
Scenario C	0,00%	100%	0,00%	0,30%	0,00%	0,00%	0,00%	0,00%	3510
Scenario D	0,00%	0,00%	100%	0,00%	0,00%	0,00%	0,00%	0,00%	3510
Scenario E	0,00%	0,00%	0,00%	99,60%	0,00%	0,00%	0,00%	0,00%	3510
Scenario F	0,00%	0,00%	0,00%	0,00%	99,50%	0,00%	0,00%	0,00%	3510
Scenario G	0,00%	0,00%	0,00%	0,00%	0,00%	100%	0,00%	0,00%	3510
Scenario H	0,00%	0,00%	0,00%	0,00%	0,00%	0,00%	100,00%	0,10%	3510
Scenario I	0,00%	0,00%	0,00%	0,00%	0,00%	0,00%	0,00%	99,50%	3510
Correct predicted values	3495	3498	3510	3522	3510	3510	3508	3527	28080
Overall Prediction 99.9%									

3. Discussion

So as not to be repetitive, in this chapter the detailed results of the most relevant scenarios and an overview of all scenarios will be discussed, at the end a table which summarizes all the results of all scenarios will be shown.

Table 13 summarizes the results obtained referring to figure 16 in scenario A, where the first configuration of retroreflective foils (red and green) has been used.

Table 13	**RMS value**	**Max. error (in degrees)**	**Min. error (in degrees)**	**Num. of errors above/below ±1°**	**Percentage of errors above/below ±1°**
RUN1	0.50	7	-1	4	1.14
RUN2	0.32	2	-1	1	0.28
RUN3	0.38	3	-1	1	0.28
RUN4	0.45	3	-3	4	1.14
RUN5	0.50	3	-2	10	2.85
RUN6	0.60	8	-1	3	0.85
RUN7	0.47	2	-2	2	0.57
RUN8	0.68	8	-3	6	1.71
RUN9	0.68	8	-1	5	1.42
RUN10	0.57	3	-2	6	1.71

Taking into account that according to the datasheet of the servomotor [27] in charge of the rotation of the robotic arm (joint 4), which is our previously mentioned ground truth, has a precision of ± 1 °, we can determine that the number of errors above or below ± 1 ° is quite low (a maximum of 10 errors for the 350 ° of rotation). One of the most notable data is that the maximum and minimum errors are + 8 ° and -3 ° respectively, and they always occur in the same range of degrees of rotation (between -140 ° and -125 °). In order to understand the reason for this event, it must be taken into account that one of the relationships of the amount of reflected light is the area of the retroreflective foils on which the light falls and is reflected. Other characteristics on which the amount of reflected light depends are the reflectivity of the material, the angle of incidence of the light, etc.

Figure 53 shows graphically how, from the point of view of the photodiode, in the red and green wristband configuration, two different rotation angles figure 53a and figure 53b can reflect the same amount of light as they have equivalent surfaces.

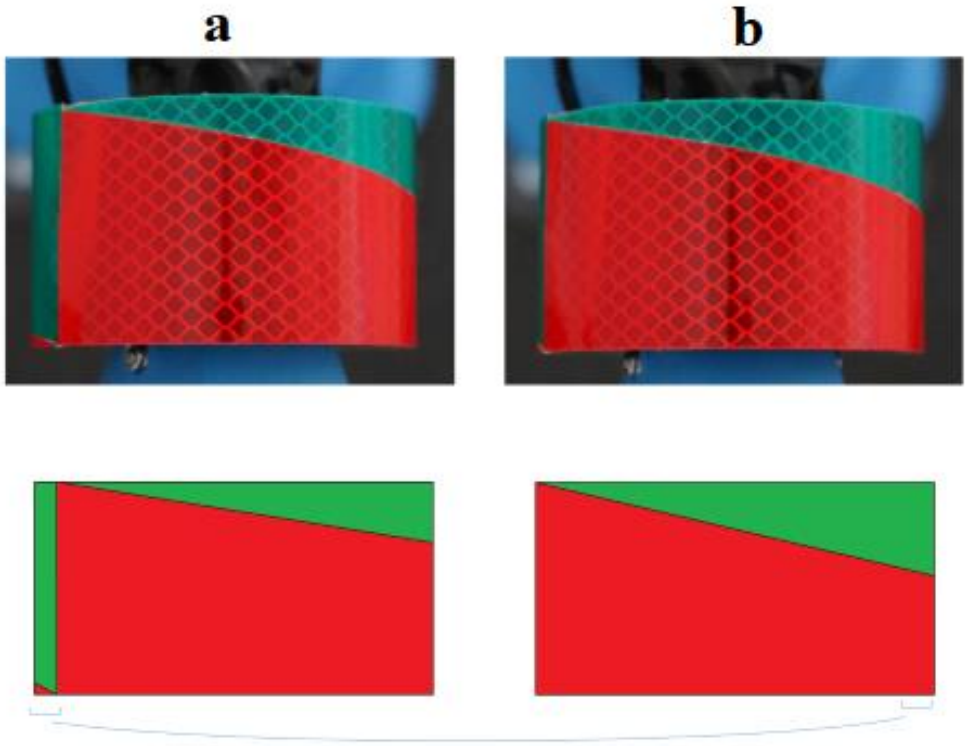

Figure 53 Equivalence of areas in two different positions seen from the photodiode

This is the main reason why a small piece of green retroreflective foil has been replaced by blue foil to create the red, green and blue foil configuration. In this way, we avoid that in the 350 degrees of rotation, the photodiode is faced to the same area for all the colours used.

Table 14 summarizes the results obtained in scenario B, where the second wristband configuration is used. A great improvement can be seen in terms of maximum and minimum errors compared to the previous scenario, in addition taking the tolerance of the servomotor into account , the results could be classified as almost perfect for predicting the rotation angle in this scenario. Thus, demonstrating that scenario B solves the error peaks present in scenario A.

Table 14	RMS value	Max. error (in degrees)	Min. error (in degrees)	Num. of errors above/below ±1°	Percentage of errors above/below ±1°
RUN1	0.23	1	-1	0	0.00
RUN2	0.30	1	-1	0	0.00
RUN3	0.20	1	-1	0	0.00
RUN4	0.26	1	-1	0	0.00
RUN5	0.21	1	-1	0	0.00
RUN6	0.31	2	-1	1	0.28
RUN7	0.18	1	-1	0	0.00
RUN8	0.34	2	-1	2	0.57
RUN9	0.18	1	-1	0	0.00
RUN10	0.34	2	-1	2	0.57

Table 15 summarizes the results obtained for scenario D, where, as previously mentioned, ambient light is present during the experiment. Again, the results are excellent, with a maximum and minimum error of +2° and -1° respectively, and almost no error above and below ± 1 °.

Table 15	RMS value	Max. error (in degrees)	Min. error (in degrees)	Num. of errors above/below ±1°	Percentage of errors above/below ±1°
RUN1	0.24	1	-1	0	0.00
RUN2	0.46	1	-1	0	0.00
RUN3	0.36	1	-1	0	0.00
RUN4	0.46	2	-1	1	0.28
RUN5	0.41	0	-1	0	0.00
RUN6	0.41	1	-1	0	0.00
RUN7	0.54	1	-1	0	0.00
RUN8	0.45	1	-1	0	0.00
RUN9	0.51	0	-1	0	0.00
RUN10	0.55	1	-1	0	0.00

Comparing table 14 and 15 we can clearly show that with this wristband configuration the same almost perfect results can be obtained.

Table 16 summarizes the results obtained for the B- I scenario, which as can be seen directly in figure 52 shows an error that does not meet the objectives of this project at all.

Table 16	RMS value	Max. error (in degrees)	Min. error (in degrees)	Num. of errors above/below ±1°	Percentage of errors above/below ±1°
RUN1	3.35	6	-11	183	52.14
RUN2	3.71	6	-12	187	53.28
RUN3	3.59	6	-12	188	53.56
RUN4	3.63	6	-12	187	53.28
RUN5	3.61	5	-12	191	54.42
RUN6	3.63	5	-12	191	54.42
RUN7	3.67	6	-12	189	53.85
RUN8	3.65	5	-12	187	53.28
RUN9	3.67	5	-12	190	54.13
RUN10	3.68	5	-12	189	53.85

That is why a differentiation in between scenarios with the RGB wristband is needed. Again, as shown in the overall scenario, using the KNN algorithm we cannot only distinguish between the degrees of rotation of the robotic arm, but we can also distinguish between the current scenarios with a prediction of 99.9% as shown in table 12. Thus, dividing the process into 2 steps. the first step consists of the differentiation of the scenario in which the experiment has been conducted, and the second step consists of determining the angle of rotation of the arm. Figure 54 graphically shows this workflow outlining the application of VLS technology in the scope of this document.

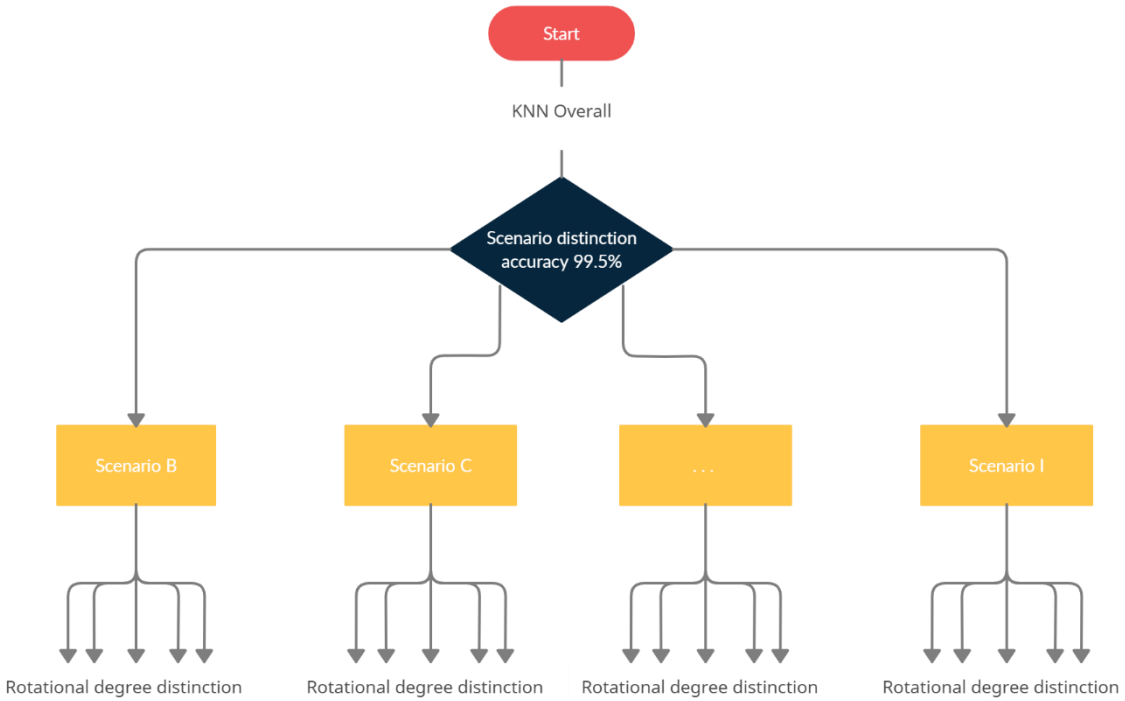

Figure 54 Rotation angle determination scheme.

The following table (table 17) shows a general perspective of the results obtained in each scenario

Table 17

Scenario	RMS value	Max. error (in degrees)	Min. error (in degrees)	Num. of errors above/below ±1°
RG	**A**	0,52	8	-3	42
RGB Lights ON	**B**	0,44	2	-1	1
RGB Tilt +5°	**C**	0,45	4	-4	19
RGB Tilt +10°	**D**	0,91	16	-1	113
RGB Tilt -5°	**E**	0,24	3	-2	6
RGB Tilt -10°	**F**	0,85	5	-4	311
RGB Azimuth +5°	**G**	0,22	1	-1	0
RGB Azimuth -5°	**H**	0,85	1	-1	0
RGB Lights Off	**I**	0,26	2	-1	5
RGB (Lights Off Train - Lights On Test/	**B - I**	3,62	6	-12	1882

4. Materials and methods

4.1 Materials

The robot was obtained from the supplier niryo (https://niryo.com/). The retroreflective foils were obtained from the supplier 3M. The VLS unit 2.0 was built by the smart connected lightning research group, MATERIALS institute JOANNEUM RESEARCH in Pinkafeld (https://www.joanneum.at/materials). The FPGA Ultra-V2 Board was obtained from the vendor AVNET (https://www.avnet.com/wps/portal/us/products/new-product-introductions/npi/aes-ultra96-v2/) [28]. The power supply used in the experiments is a Keysight, model E36313A.

All images were captured with a Sony Alpha 7 III camera. Photonic measurements were measured with UPRtek MK350S PREMIUM hand spectrometer.

The metal structure has been custom manufactured in the laboratory.

4.2 Data collection & processing methodology

All the values obtained by the RGB photodiode are sent by the ADC to the AXI register of the Ultra-V2 board FPGA (please see figure 6). Through a serial port of a standard laptop, 500 absolute values from the FPGA´s SOC for each angle of rotation are collected and then stored in the computer as a .csv file. Once 351 .csv files have been obtained (350 ° of rotation), the process is repeated until the 20 runs are obtained.

For the looping of the 20 runs, file creation and storage, batch scripts have been used in addition to PowerShell scripts.

The control of the robot has been carried out through the Raspberry PI3 integrated in it. By utilizing a python script controlled by a batch script, the moves of the robotic arm were synchronized with the data storage.

Once all the values are stored, utilizing the octave software, for each .csv file of each run the mean value and the absolute values, were processed, in addition to representing them graphically. For each run consequently a .csv file is created containing all the previously utilized absolute and relative values.

The 20 files that contain the information of the mean value for each angle of rotation for the 20 runs are divided into 2 groups, the first 10 files are merged through a python script for the training phase. The following 10 files go through the same process to be used for the testing phase in the machine learning process.

For the machine learning process, the Orange Data Mining software (https://orangedatamining.com/) has been used and the algorithm used is the K-nearest neighbour (KNN) with a value of k = 1.

The output values of the algorithm are then again processed by the octave software in order to graphically represent the error obtained.

The figure 55 shows the data collection and process diagram for each scenario.

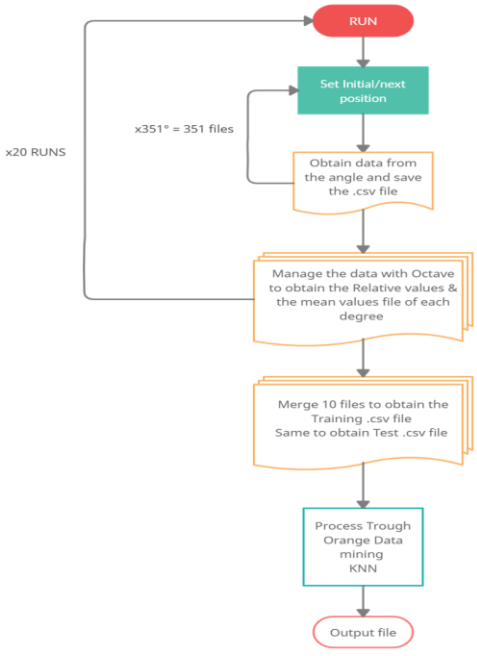

Figure 55 Flowchart of data collection and process.

5. References

[1] A. Yahya, "4th Industrial revolution: The future of machining," 2017 4th International Conference on Information Technology, Computer, and Electrical Engineering (ICITACEE), 2017, pp. 3-4, doi: 10.1109/ICITACEE.2017.8257664.

[2] J. M. Tien, "Towards the next industrial revolution," 2012 4th IEEE International Symposium on Logistics and Industrial Informatics, 2012, pp. 13-14, doi: 10.1109/LINDI.2012.6319480.

[3] M. Franz, and F. P. Wenzl, "Critical review on life cycle inventories and environmental assessments of LED-lamps", Crit. Rev. Environ. Sci. Technol. vol. 47, pp. 2017-2078, 2017

[4] Y. -C. Lee, J. -L. Lai, C. -H. Yu and C. -S. A. Gong, "The high-efficiency LED driver for visible light communication applications," 2016 Eighth International Conference on Ubiquitous and Future Networks (ICUFN), 2016, pp. 56-58, doi: 10.1109/ICUFN.2016.7536979.

[5] C. Hyunchae et al., "A Wide-Area Coverage 35 Gb/S Visible Light Communications Link for Indoor Wireless Applications", Nature Scientific reports, vol. 9, no. 1, pp. 1-8, Mar. 2019.

[6] H. Li et al., "A Fast and High-Accuracy Real-Time Visible Light Positioning System Based on Single LED Lamp With a Beacon," in IEEE Photonics Journal, vol. 12, no. 6, pp. 1-12, Dec. 2020, Art no. 7906512, doi: 10.1109/JPHOT.2020.3032448.

[7] W. Xu, J. Wang, H. Shen, H. Zhang and X. You, "Indoor Positioning for Multiphotodiode Device Using Visible-Light Communications," in IEEE Photonics Journal, vol. 8, no. 1, pp. 1-11, Feb. 2016, Art no. 7900511, doi: 10.1109/JPHOT.2015.2513198.

[8] A. P. Weiss, S. Z. Rad and F. P. Wenzl, "Pose detection with backscattered visible light sensing utilizing a single RGB photodiode: A model based feasibility study," 2020 International Wireless Communications and Mobile Computing (IWCMC), 2020, pp. 137-142, doi: 10.1109/IWCMC48107.2020.9148177.

[9] P. H. Pathak, X. Feng, P. Hu and P. Mohapatra, "Visible Light Communication, Networking, and Sensing: A Survey, Potential and Challenges," in IEEE Communications Surveys & Tutorials, vol. 17, no. 4, pp. 2047-2077, Fourthquarter 2015, doi: 10.1109/COMST.2015.2476474.

[10] K. Warmerdam, A. Pandharipande, D. Caicedo and M. Zuniga, "Visible Light Communications for Sensing and Lighting Control," in IEEE Sensors Journal, vol. 16, no. 17, pp. 6718-6726, Sept.1, 2016, doi: 10.1109/JSEN.2016.2585199.

[11] T. C. Wu et al., "Tricolor R/G/B laser diode based eye-safe white lighting communication beyond 8 Gbit/s", Sci. Rep., vol. 7, pp. 11, 2017.

[12] S. Z. Rad, K. Madane, A. P. Weiss and F. P. Wenzl, "A Channel Modeling Procedure for Visible Light Sensing," 2020 43rd International Spring Seminar on Electronics Technology (ISSE), 2020, pp. 1-6, doi: 10.1109/ISSE49702.2020.9120940.

[13] A. Mukherjee, "Secret-Key Agreement for Security in Multi-Emitter Visible Light Communication Systems," in IEEE Communications Letters, vol. 20, no. 7, pp. 1361-1364, July 2016, doi: 10.1109/LCOMM.2016.2558562.

[14] K. Warmerdam, A. Pandharipande and D. Caicedo, "Connectivity in IoT indoor lighting systems with visible light communications," 2015 IEEE Online Conference on Green Communications (OnlineGreenComm), 2015, pp. 47-52, doi: 10.1109/OnlineGreenCom.2015.7387378.

[15] M. Kaholokula, "Reusing ambient light to recognize hand gestures" in , Hanover, NH, USA:Undergraduate thesis, Dartmouth College, 2016.

[16] R. Bloom, M. Zuniga, Q. Wang and D. Giustiniano, "Tweeting with Sunlight: Encoding Data on Mobile Objects," IEEE INFOCOM 2019 - IEEE Conference on Computer Communications, 2019, pp. 1324-1332, doi: 10.1109/INFOCOM.2019.8737410.

[17] D. Konings, N. Faulkner, F. Alam, E. M. . -K. Lai and S. Demidenko, "FieldLight: Device-Free Indoor Human Localization Using Passive Visible Light Positioning and Artificial Potential Fields," in IEEE Sensors Journal, vol. 20, no. 2, pp. 1054-1066, 15 Jan.15, 2020, doi: 10.1109/JSEN.2019.2944178.

[18] A. A. Al-Hameed, S. H. Younus, A. T. Hussein, M. T. Alresheed and J. M. H. Elmirghani, "LiDAL: Light Detection and Localization," in *IEEE Access*, vol. 7, pp. 85645-85687, 2019, doi: 10.1109/ACCESS.2019.2925076.

[19] S. K. J. J. S. e. a. Lee, “Evaluation of visible light communication channel delay profiles for automotive applications.,” 27 12 2012. [Online]. Available: https://jwcn-eurasipjournals.springeropen.com/articles/10.1186/1687-1499-2012-370#citeas. [Accessed 22 03 2022].

[20] A. Navlani, “Datacamp,” 2 08 2018. [Online]. Available: https://www.datacamp.com/tutorial/k-nearest-neighbor-classification-scikit-learn. [Accessed 21 3 2022].

[21] K. Madane, A. P. Weiss, S. Schantl, E. Leitgeb and F. P. Wenzl, "Machine Learning Assisted Visible Light Sensing of the Rotation of a Robotic Arm," in IEEE Access, vol. 9, pp. 130721-130736, 2021, doi: 10.1109/ACCESS.2021.3112297.

[22] Kinbright, “APS5130PD7C-P22 RGB Color Sensor Datasheet,” [Online]. Available: https://www.kingbrightusa.com/images/catalog/SPEC/APS5130PD7C-P22.pdf. [Accessed 30 05 2022].

[23] N. SAS, “Niryo One user manual,” [Online]. Available: https://niryo.com/docs/niryo-one/user-manual/complete-user-manual/. [Accessed 03 03 2022].

[24] 3M, “3M Diamond Grade DG3 Reflective Sheeting Series 4000 Product Bulletin 4000,” January 2020. [Online].

[25] UPRtek Corp., “MK350S Premium Specs.,” [Online]. Available: https://www.uprtek.com/en/product/spectrometers/mk350s-premium. [Accessed 2 9 2021].

[26] University of Ljubljana, “Orange data mining,” [Online]. Available: https://orangedatamining.com/. [Accessed 12 11 2021].

[27] ROBOTIS, “Dynamixel XL430-W250 Specifications,” [Online]. Available: https://emanual.robotis.com/docs/en/dxl/x/xl430-w250/. [Accessed 20 8 2021].

[28] AVNET Inc., “Ultra96-V2 Single Board Computer User’s Guide,” [Online]. Available: https://www.avnet.com/wps/portal/us/products/avnet-boards/avnet-board-families/ultra96-v2/ultra96-board-family/!ut/p/z1/vVVdU6MwFP0rvPiYyeUrhcdQkRah2la08LKT8mGjBSqNaP31G7vu7jhjy-4o5iEfd07OvedM5gYneIGTirX8lgleV2wtz3FCfni2OVaHQwg9xx_A9JJGJLAnejgCfLMHBNR2RxS. [Accessed 20 7 2021].

A. P. Weiss, K. Madane, S. Z. Rad and F. P. Wenzl, "Implementation of a Cost-Efficient Passive Visible Light Sensing Approach for the Determination of Surface Colors," 2019 Austrochip Workshop on Microelectronics (Austrochip), 2019, pp. 81-86, doi: 10.1109/Austrochip.2019.00026.

[29] Cree Inc., “Product family datasheet,” [Online]. Available: https://cree-led.com/media/documents/XLampMCE.pdf. [Accessed 21 04 2022].